Sunyaev-Zel'dovich observations of galaxy clusters out to the virial radius with the Arcminute Microkelvin Imager

Zwart, J.T.L.; Feroz, F.; Davies, M.L.; Franzen, T.M.O.; Grainge, K.J.B.; Hobson, M.P.; ... ; Waldram, E.M.

Citation

Zwart, J. T. L., Feroz, F., Davies, M. L., Franzen, T. M. O., Grainge, K. J. B., Hobson, M. P., ... Waldram, E. M. (2011). Sunyaev-Zel'dovich observations of galaxy clusters out to the virial radius with the Arcminute Microkelvin Imager. *Monthly Notices Of The Royal Astronomical Society*, *418*(4), 2754-2772. doi:10.1111/j.1365-2966.2011.19665.x

Monthly Notices
of the
ROYAL ASTRONOMICAL SOCIETY

Mon. Not. R. Astron. Soc. **418,** 2754–2772 (2011)
doi:10.1111/j.1365-2966.2011.19665.x

Sunyaev–Zel'dovich observations of galaxy clusters out to the virial radius with the Arcminute Microkelvin Imager★

AMI Consortium: Jonathan T. L. Zwart,[1,2]† Farhan Feroz,[1] Matthew L. Davies,[1] Thomas M. O. Franzen,[1] Keith J. B. Grainge,[1,3] Michael P. Hobson,[1] Natasha Hurley-Walker,[1] Rüdiger Kneissl,[1,4] Anthony N. Lasenby,[1,3] Malak Olamaie,[1] Guy G. Pooley,[1] Carmen Rodríguez-Gonzálvez,[1] Richard D. E. Saunders,[1,3] Anna M. M. Scaife,[1,5] Paul F. Scott,[1] Timothy W. Shimwell,[1] David J. Titterington[1] and Elizabeth M. Waldram[1]

[1]*Astrophysics Group, Cavendish Laboratory, J. J. Thomson Avenue, Cambridge CB3 0HE*
[2]*Columbia Astrophysics Laboratory, Columbia University, 550 West 120th Street, New York, NY 10027, USA*
[3]*Kavli Institute for Cosmology Cambridge, Madingley Road, Cambridge CB3 0HA*
[4]*Joint ALMA Office, Av El Golf 40, Piso 18, Santiago, Chile*
[5]*Dublin Institute for Advanced Studies, 31 Fitzwilliam Place, Dublin 2, Ireland*

Accepted 2011 August 19. Received 2011 August 17; in original form 2010 August 2

ABSTRACT

We present observations using the Small Array of the Arcminute Microkelvin Imager (AMI; 14–18 GHz) of four Abell and three MACS clusters spanning 0.171–0.686 in redshift. We detect Sunyaev–Zel'dovich (SZ) signals in five of these without any attempt at source subtraction, although strong source contamination is present. With radio-source measurements from high-resolution observations, and under the assumptions of spherical β-model, isothermality and hydrostatic equilibrium, a Bayesian analysis of the data in the visibility plane detects extended SZ decrements in all seven clusters over and above receiver noise, radio sources and primary cosmic microwave background imprints. Formal Bayesian evidence ratios range from 10^{11}:1 to 10^{43}:1 for six of the clusters and 3000:1 for one with substantially fewer data than the others. We present posterior probability distributions for, e.g., total mass and gas fraction averaged over radii internal to which the mean overdensity is 1000, 500 and 200, r_{200} being the virial radius. Reaching r_{200} involves some extrapolation for the nearer clusters but not for the more distant ones. We find that our estimates of gas fraction are low (compared with most in the literature) and decrease with increasing radius. These results appear to be consistent with the notion that gas temperature in fact falls with distance (away from near the cluster centre) out to the virial radius.

Key words: methods: data analysis – galaxies: clusters: general – cosmic background radiation – cosmology: observations – radio continuum: general.

1 INTRODUCTION

The Sunyaev–Zel'dovich (SZ) effect (Sunyaev & Zeldovich 1970, 1972) is the inverse-Compton scattering of the cosmic microwave background (CMB) radiation by hot, ionized gas in the gravitational potential well of a cluster of galaxies (see Birkinshaw 1999; Carlstrom, Holder & Reese 2002, for reviews). The effect is useful in a number of ways for the study of galaxy clusters; here we are concerned with two in particular. First, because the SZ effect arises from a scattering process, a cluster at one redshift will produce the same observed SZ surface brightness as an identical cluster at any other redshift, so that the usual sensitivity issue of high-redshift observation does not arise. Secondly, since the SZ surface brightness is proportional to the line-of-sight integral of pressure through the cluster, the SZ signal is less sensitive to concentration than the X-ray bremsstrahlung signal; one corollary of this is that the ratio SZ-sensitivity/X-ray-sensitivity increases with distance from the cluster centre so that with SZ one can probe out to, say, the virial radius, provided the SZ telescope is sensitive to sufficiently large angular scales.

★We request that any reference to this paper cites 'AMI Consortium: Zwart et al. 2001'.

†Issuing author – E-mail: jtlz2@astro.columbia.edu

Table 1. AMI (AMI Consortium: Zwart et al. 2008) technical summary.

	SA	LA
Antenna diameter	3.7 m	12.8 m
Number of antennas	10	8
Baseline lengths (current)	5–20 m	18–110 m
Primary beam (15.7 GHz)	20.1 arcmin	5.5 arcmin
Synthesized beam	≈3 arcmin	≈30 arcsec
Flux sensitivity	30 mJy $\mathrm{s}^{1/2}$	3 mJy $\mathrm{s}^{1/2}$
Observing frequency	13.9–18.2 GHz	
Bandwidth	4.3 GHz	
Number of channels	6	
Channel bandwidth	0.72 GHz	

SZ decrements are faint, however, and can be contaminated or obliterated by other sources of radio emission. A range of new, sensitive instruments has been brought into use to capitalize on the science from SZ observations. Among these instruments, which employ different strategies to maximize sensitivity and minimize confusion, are Atacama Cosmology Telescope (ACT; Hincks et al. 2010; Hand et al. 2011; Sehgal et al. 2011; Swetz et al. 2011), Arcminute Microkelvin Imager (AMI; AMI Collaboration: Barker et al. 2006; AMI Collaboration: Hurley-Walker et al. 2011; AMI Collaboration: Rodriguez-Gonzalvez et al. 2011a; AMI Collaboration: Rodriguez-Gonzalvez 2011b; AMI Collaboration: Shimwell et al. 2011; AMI Consortium: Zwart et al. 2008), the Yuan-Tseh Lee Array for Microwave Background Anisotropy (AMiBA; Ho et al. 2009; Wu et al. 2009; Huang et al. 2010; Liao et al. 2010), the Atacama Pathfinder Experiment (APEX; Dobbs et al. 2006), One Centimetre Receiver Array (OCRA; Lancaster et al. 2007), South Pole Telescope (SPT; Carlstrom et al. 2009; Staniszewski et al. 2009; Plagge et al. 2010), the Combined Array for Research in Millimeter-Wave Astronomy (CARMA) and Sunyaev–Zel'dovich Array (SZA; Muchovej et al. 2007; Mroczkowski et al. 2009). In the case of AMI, two separate interferometer arrays are used, the Small Array (SA) having short baselines sensitive to SZ and radio sources, and the Large Array (LA) with baselines sensitive to the radio sources alone and thus providing source subtraction for the SA. Key parameters of the SA and LA are shown in Table 1.

The SA was built first. Partly to test it while the LA was being completed, we used the SA to observe Galactic supernova remnants and likely regions of spinning dust (AMI Consortium: Scaife et al. 2008, 2009a,b; AMI Consortium: Hurley-Walker et al. 2009a,b) bright enough not to need source subtraction. However, we also wanted to begin SZ observation, test our algorithms to extract SZ signals in the presence of radio sources, CMB primary anisotropies and receiver noise, and begin our SZ science programme. To do this required the use of long-baseline data from the 15-GHz Ryle Telescope (RT; see e.g. Grainge et al. 1996; Grainger et al. 2002, for source-subtraction discussion) taken in the past; this needs caution because of radio-source variability (see e.g. Bolton et al. 2006; Sadler et al. 2006; AMI Consortium: Franzen et al. 2009), but our data-analysis algorithm allows for variability and in fact we were able to use some data from the LA, which, at the time, was only partially commissioned. Here we present, in the first part of this programme, SZ measurements of seven clusters of galaxies, each of redshift z and of X-ray luminosity L_{X}.

We assume a concordance Λ cold dark matter cosmology, with $\Omega_{\mathrm{m}} = 0.3$, $\Omega_{\Lambda} = 0.7$, $\Omega_{\mathrm{k}} = 0$, $\Omega_{\mathrm{b}} = 0.041$, $w_0 = -1$, $w_a = 0$, $\sigma_8 = 0.8$ and $H_0 = 70\,\mathrm{km\,s^{-1}\,Mpc^{-1}}$. However, in plots of probability distribution, we explicitly include the dimensionless Hubble parameter, defined as $h \equiv H_0/(100\,\mathrm{km\,s^{-1}\,Mpc^{-1}})$, to allow comparison with other work.

All coordinates are J2000 epoch. Our convention for spectral index α (except in Section 6 for MACS J0717+37) is $S_\nu \propto \nu^{-\alpha}$, where S is flux density and ν is frequency. We write the radius internal to which the mean density is a times the critical density ρ_{crit} at the particular redshift as r_a, the total mass (gas plus dark matter) internal to r_a as M_a and the gas mass internal to r_a as $M_{\mathrm{gas},a}$.

2 CLUSTER SELECTION AND RT OBSERVATION

We used the NOrthern *ROSAT* All-Sky Survey (NORAS; Böhringer et al. 2000) catalogue as a source of low-redshift ($z < 0.3$) clusters and the MAssive Cluster Survey (MACS; Ebeling, Edge & Henry 2001; Ebeling et al. 2007, 2010) to give secure, more distant clusters that provide some filling-out of the L_{X}–z plane. We restricted redshifts to $z > 0.1$ to avoid resolving out SZ signals and luminosity to $L_{\mathrm{X}} > 7 \times 10^{37}$ W (0.1–2.4 keV, rest frame).

We restricted declinations to greater than 20° since the RT had only east–west baselines, and further excluded clusters which we knew, from the National Radio Astronomy Observatory Very Large Array Sky Survey (Condon et al. 1998) or from archival RT data, would be too contaminated by radio sources. Details of the resulting seven clusters in this work are given in Table 2; this is *not* a complete sample of clusters and other clusters could have been chosen instead. Source surveying of the remaining clusters with the compact array of the RT – note that this array contained five of the eight antennas of the LA – was then carried out as follows.

The RT data were obtained between 2004 and 2006. Each cluster field was surveyed in two ways: with a wide shallow raster and a deep central one. The wide shallow raster comprised a hexagonal close-packed raster of 11 × 12 pointings on a 5-arcmin grid, with a dwell time at each pointing of 5 min; the aim was to identify relatively bright radio sources in the direction of an SA pointing. The centre of each cluster was followed up with a hexagon of 7 × 12 h RT pointings, on a 5-arcmin grid, in order to detect faint sources near the target cluster.

Data were reduced, and point-source positions and fluxes extracted, using procedures developed for the The Ninth Cambridge (9C) Survey of Radio Sources and outlined in Waldram et al. (2003). The source data are given in Table 3.

At this point, we give examples from the literature of other SZ observations of these clusters. Grainger et al. (2002) and Bonamente et al. (2004) show A611; Carlstrom, Joy & Grego (1996) and Saunders et al. (2003) show A773; AMI Collaboration: Barker et al. (2006) and Mroczkowski et al. (2009) show A1914; Birkinshaw & Hughes (1994), Tsuboi et al. (1998), Jones et al. (2005) and Lancaster et al. (2007) show A2218; and LaRoque et al. (2003) show MACS J0717+37 and MACS J0744+39. See also e.g. Zemcov et al. (2007).

3 AMI OBSERVATION AND REDUCTION

The seven clusters were observed with the SA between 2007 October and 2008 January. Each cluster typically had 25 h of SA observing on the sky (though A2218, MACS J0308+26 and MACS J0717+27 had some 70 h). The *uv*-coverage is well filled (Fig. 1) all the way down to ≈180λ, corresponding to a maximum angular scale of ≈10 arcmin.

Table 2. Clusters in this work. Temperatures, redshifts and X-ray luminosities are from (1) LaRoque et al. (2006), (2) Balestra et al. (2007), (3) Ebeling et al. (2007), (4) Böhringer et al. (2000), (5) Struble & Rood (1999), (6) Ebeling (private communication). The map noise indicated is for a SA naturally weighted map with all baselines and no source subtraction. The integration times t_{int} are on-sky times, and do not account for variations in system temperature with airmass or poor weather, or for the amount of data flagged due to, for example, shadowing.

Cluster	RA (J2000)	Dec. (J2000)	z	T (keV)	L_{X}(10^{37} W)	t_{int} (h)	rms (μJy)
A611	08 00 59.40	+36 03 01.0	0.288 (4)	$6.79^{+0.41}_{-0.38}$ (1)	8.63 (4)	23.8	140
A773	09 17 52.97	+51 43 55.5	0.217 (5)	$8.16^{+0.56}_{-0.52}$ (1)	12.11 (4)	23.8	160
A1914	14 26 02.15	+37 50 05.8	0.171 (4)	$9.48^{+0.35}_{-0.29}$ (1)	15.91 (4)	20.9	140
A2218	16 35 52.80	+66 12 50.0	0.171 (4)	$7.80^{+0.41}_{-0.37}$ (1)	8.16 (4)	62.4	90
MACS J0308+26	03 08 55.40	+26 45 39.0 (6)	0.352 (6)	$11.2^{+0.7}_{-0.7}$ (2)	15.89 (6)	86.6	140
MACS J0717+37	07 17 30.00	+37 45 00.0 (6)	0.546 (3)	$11.6^{+0.5}_{-0.5}$ (3)	25.33 (6)	23.8	160
MACS J0744+39	07 44 48.00	+39 27 00.0 (6)	0.698 (3)	$8.14^{+0.80}_{-0.72}$ (1)	17.16 (6)	71.8	320

Table 3. Contaminating sources. Flux density values here are taken from the map plane. W denotes RT wide, shallow raster (11 × 12 pointings, 5-min integration per pointing), while H denotes an RT deep hexagon (7 pointings, 12-h integration per pointing). SA(L) refers to long baselines of the SA. Fluxes from RT shallow raster observations were boosted by 10 per cent to account for pointing errors (Waldram et al. 2003). 9C denotes data from 9C pointed observations (Waldram et al. 2003). The S-uncertainty values represent receiver noise taking into account primary beam attenuation; RT map noises can have additional noise contribution from raster striping. For explanation of RT/LA for source 2 in A1914, see Section 5.1.2.

Cluster		RA (J2000)	Dec. (J2000)	Array	Mode	(mJy)
A611	1	08 00 43.28	+36 14 00.9	SA		5.5 ± 1.7
	2	08 00 09.91	+36 04 15.4	SA		4.4 ± 1.3
A773	1	09 18 38.29	+51 50 25.0	SA		4.4 ± 0.6
	2	09 17 06.13	+51 44 54.9	SA		3.4 ± 0.4
	3	09 17 57.02	+51 45 08.0	LA		0.12 ± 0.03
	4	09 18 01.33	+51 44 13.1	LA		0.32 ± 0.05
	5	09 17 45.31	+51 43 04.6	LA		0.22 ± 0.03
	6	09 17 55.58	+51 43 01.1	LA		0.19 ± 0.03
	7	09 17 50.67	+51 41 06.1	LA		0.31 ± 0.05
A1914	1	14 25 10.21 (SA)	+37 52 35.1 (SA)	SA(L)		4.2 ± 0.4
	2	14 27 24.75 (RT)	+37 46 33.8 (RT)	RT/LA		9.7 ± 1.0 (LA)
	3	14 25 48.02	+37 47 50.3	LA		1.0 ± 0.3
	4	14 25 40.84	+37 45 50.4	LA		3.7 ± 0.4
	5	14 25 50.53	+37 45 10.3	LA		0.61 ± 0.18
	6	14 25 58.53	+37 44 00.1	LA		0.60 ± 0.18
A2218	1	16 35 47.24	+66 14 46.9	RT	H	1.9 ± 0.6
	2	16 36 15.74	+66 14 27.0	RT	H	1.9 ± 0.6
	3	16 35 22.14	+66 13 20.6	RT	W	5.6 ± 2
	4	16 33 18.18	+66 00 50.6	RT	W	10 ± 3
	5	16 35 39.78	+65 58 12.0	RT	W	11 ± 3
	6	16 34 46.36	+65 55 18.6	RT	W	13 ± 4
	7	16 37 22.56	+66 21 18.4	SA(L)		5.2 ± 1.6
MACS J0308+26	1	03 09 42.02	+26 56 30.3	9C	W	8 ± 2
	2	03 08 56.52	+26 44 54.0	SA(L)		2.4 ± 0.7
	3	03 09 40.14	+26 37 23.6	SA(L)		2.9 ± 0.9
MACS J0717+37	1	07 17 36.09	+37 45 56.3	RT	H	2.1 ± 0.3
	2	07 17 35.91	+37 45 11.2	RT	H	1.8 ± 0.3
	3	07 17 37.14	+37 44 23.1	RT	H	3.9 ± 0.8
	4	07 17 41.06	+37 43 15.2	RT	H	2.5 ± 0.5
	5	07 18 10.51	+37 49 14.6	SA(L)		18 ± 1.4
	6	07 16 35.69	+37 39 14.2	SA(L)		4.7 ± 1.4
MACS J0744+39	1	07 44 32.95	+39 32 15.0	RT	H	2.8 ± 0.2
	2	07 44 22.30	+39 25 46.5	RT	H	1.1 ± 0.2
	3	07 43 58.76	+39 15 02.3	RT	W	52 ± 2
	4	07 43 45.99	+39 14 21.5	RT	W	8.3 ± 2

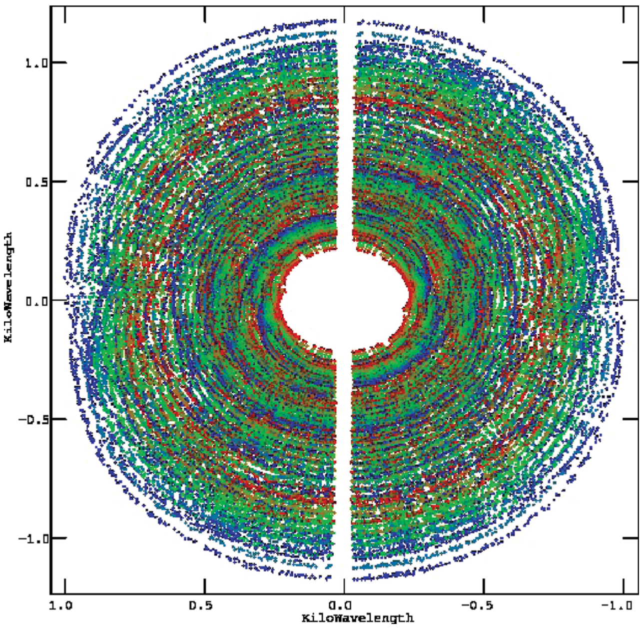

Figure 1. SA *uv*-coverage for A2218; coverages for the other clusters are very similar to this. The different colours correspond to different frequency channels.

Calibration and reduction procedures were as follows. One of our two absolute flux calibrators, 3C 286 and 3C 48, was observed immediately before or after each cluster observation. The absolute flux calibration is accurate to 5 per cent (see AMI Consortium: Hurley-Walker et al. 2009b). Each cluster observation was reduced separately using our in-house software REDUCE. An automatic reduction pipeline is in place, but all the data were examined by eye for problems. Data were flagged for shadowing, slow fringe rates, path-compensator delay errors and pointing errors. The data were flux calibrated, Fourier transformed and fringe rotated to the pointing centre. Further amplitude cuts were made in order to remove interference spikes and discrepant baselines. The amplitudes of the visibilities were corrected for variations in the system temperature with airmass, cloud and weather, and the data weights converted into Jy^{-2}. Secondary (interleaved) calibration was applied, by observing a point-source calibrator every hour, to correct for system phase drifts. The data were smoothed from 1- to 10-s samples, and calibrated UVFITS were outputted and co-added using PYFITS. Typically, 20–30 per cent of the data were discarded due to bad weather, telescope downtime and other flagging. The data were mapped in AIPS and also directly analysed in the visibility plane.

In some cases, as indicated in Table 3, it was possible to use some of the then partially commissioned LA for source subtraction, assisting with any effects of the time gap between RT and SA observations (LA calibration and reduction are very similar to that of the SA, described above). Similarly, for some sources of high flux density away from the cluster, the long baselines of the SA provided useful measurements.

3.1 Maps

We used standard AIPS tasks to produce naturally weighted SA maps with all baselines, no taper and no source subtraction. These images, after CLEANing, are shown in Fig. 2. The maps have differing noises due largely to differing integration times. Sources are evident in all the maps. In five of the maps, an extended SZ decrement is visible, despite major source contamination at the X-ray centres in the cases of A2218 and MACS J0308+26. In MACS J0717+37, there seems to be some negative signal, but the source contamination at the map centre is severe (Edge et al. 2003; Ebeling, Barrett & Donovan 2004). In MACS J0744+39, the contamination is less, but there is still only a weak decrement – but we note that the thermal noise is at least twice that of every other map.

There is a previous AMI observation of A1914: AMI Collaboration: Barker et al. (2006) show an image (without source subtraction) towards this cluster from an early phase of the SA. This image is similar to that in Fig. 2 but uses fewer, older data, has poor *uv*-coverage and has much less robust flux and phase calibration; Barker et al. use the RT for source subtraction. We have compared the Barker et al. flux densities with those of the present work for the Barker et al. sources B, C, D, G, L and O, revealing flux density differences of up to 40 per cent for the faintest source. These differences are unsurprising given variability, the high RT noise and the points above.

To illustrate source-subtracted maps, Fig. 4 contains SA maps of Abell 2218 and MACS J0717+37 with sources subtracted from the SA visibilities. These clusters present the biggest subtraction challenges of the seven clusters in this paper: strong emission close to the cluster centre along with mostly RT subtraction observations (which are necessarily insensitive and the most differing in epoch from the SA observations). The positions and fluxes used for subtraction were as in Table 3; only those sources falling inside the images in Figs 2 and 3 are shown (as crosses) in Fig. 4 (except for source 6 – see Table 4). We postpone additional information to section 6.

Subsequent analysis was carried out in the visibility plane, taking into account radio sources, receiver noise and primary CMB contamination, as we describe in the next section.

4 RESUME OF ANALYSIS

4.1 Bayesian analysis

Bayesian analysis of interferometer observations of clusters in SZ has been discussed by us previously in e.g. Hobson & Maisinger (2002), Marshall, Hobson & Slosar (2003) and Feroz et al. (2009). The advantages of this approach are as follows.

(i) One infers the quantity that one actually wants, the probability distribution of the values of parameters $\boldsymbol{\Theta}$, given the data $\boldsymbol{D}$ and some model, or hypothesis, H, via Bayes' theorem:

$$\Pr(\boldsymbol{\Theta}|\boldsymbol{D}, H) = \frac{\Pr(\boldsymbol{D}|\boldsymbol{\Theta}, H)\Pr(\boldsymbol{\Theta}|H)}{\Pr(\boldsymbol{D}|H)}. \qquad (1)$$

(ii) The likelihood $\Pr(\boldsymbol{D}|\boldsymbol{\Theta}, H)$ is the probability of the data given parameter values and a model, and encodes the constraints imposed by the observations. It includes information about noise arising from the receivers, primary CMB and unsubtracted radio sources lying below the detection level of the source-subtraction procedure.

(iii) The prior $\Pr(\boldsymbol{\Theta}|H)$ allows one to incorporate prior knowledge of the parameter values and, for example, allows one to deal fully and objectively with the contaminants such as sources (which may be variable).

(iv) The evidence $\Pr(\boldsymbol{D}|H)$ is obtained by integrating $\Pr(\boldsymbol{D}|\boldsymbol{\Theta}, H)\Pr(\boldsymbol{\Theta}|H)$ over all $\boldsymbol{\Theta}$, allowing normalization of the posterior $\Pr(\boldsymbol{\Theta}|\boldsymbol{D}, H)$. One can select different models by comparing their evidences, the process automatically incorporating Occam's razor.

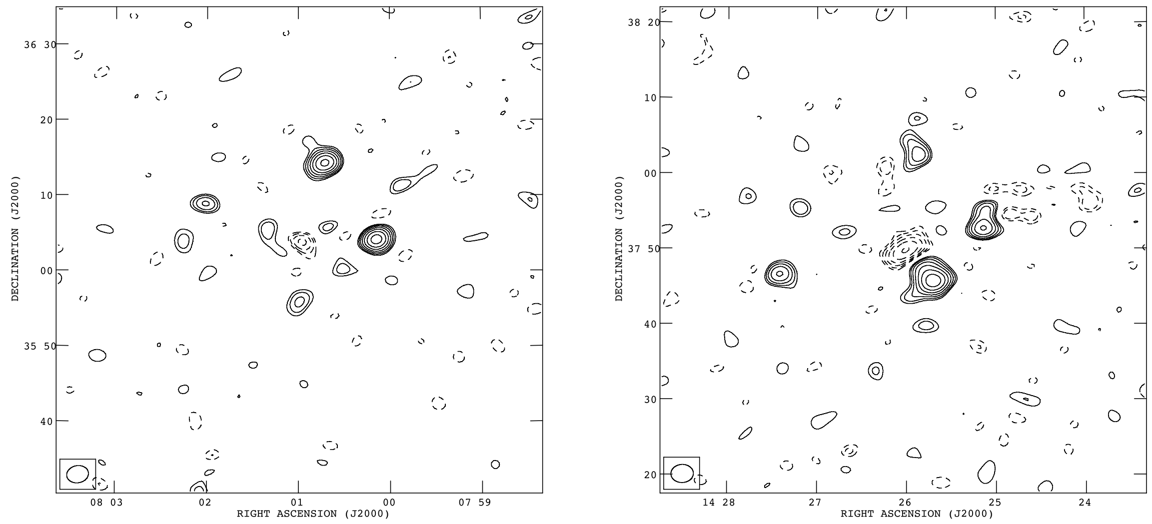

(a) A611. The 1-σ map noise is $139\,\mu$Jy beam^{-1}. Contour levels start at $\pm 280\,\mu$Jy beam^{-1}; thereafter contours are spaced by a factor of $\sqrt{2}$.

(b) A1914. The 1-σ map noise is $144\,\mu$Jy beam^{-1}. Contour levels start at $\pm 290\,\mu$Jy beam^{-1}; thereafter contours are spaced by a factor of $\sqrt{2}$.

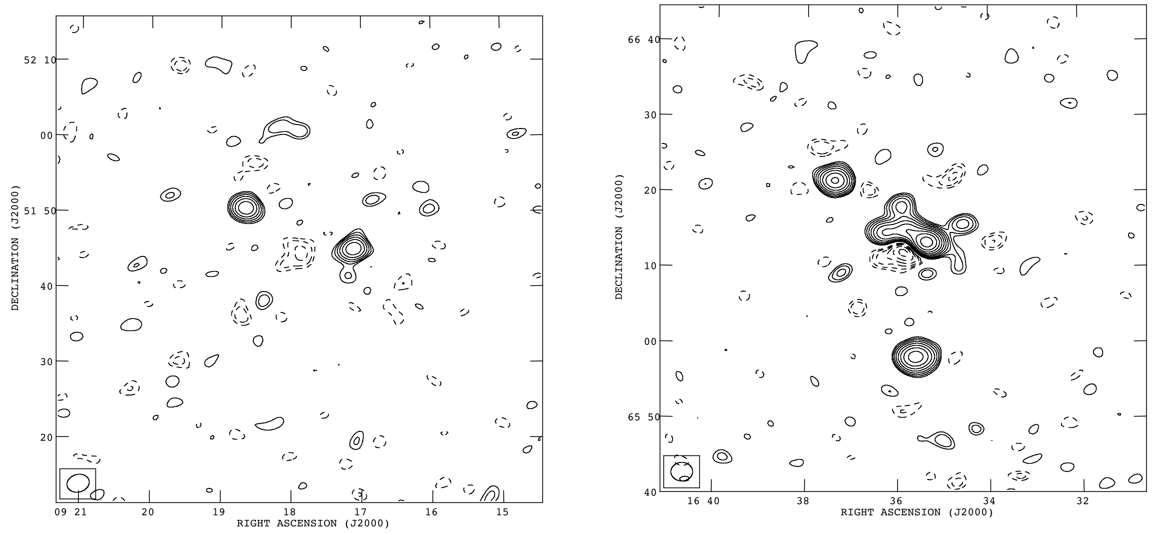

(c) A773. The 1-σ map noise is $157\,\mu$Jy beam^{-1}. Contour levels start at $\pm 310\,\mu$Jy beam^{-1}; thereafter contours are spaced by a factor of $\sqrt{2}$.

(d) A2218. The 1-σ map noise is $88\,\mu$Jy beam^{-1}. Contour levels start at $\pm 180\,\mu$Jy beam^{-1}; thereafter contours are spaced by a factor of $\sqrt{2}$.

Figure 2. SA naturally weighted, untapered, primary-beam-uncorrected maps of the Abell clusters. No source subtraction has been done. The synthesized beam is indicated in the lower left-hand corner of each image.

(v) However, performing these integrations, and sampling the parameter space, is non-trivial and can be slow. The use of the 'nested sampler' algorithm MultiNest both speeds up the sampling process significantly and, more importantly, allows one to sample from probability distributions with multiple peaks and/or large curving degeneracies (Feroz & Hobson 2008).

(vi) Throughout the whole analysis, probability distributions – with their asymmetries, skirts, multiple peaks and whatever else – are used and combined correctly, rather than discarding information (and, in general, introducing bias) by representing distributions by a mean value and an uncertainty expressed only in terms of a covariance matrix.

4.2 Physical model and assumptions

We restrict ourselves to the simplest model, by assuming a spherical β-model for isothermal (see Section 4.3), ideal cluster gas in hydrostatic equilibrium. Following e.g. Grego et al. (2001), the equation of hydrostatic equilibrium for a spherical shell of gas of density ρ

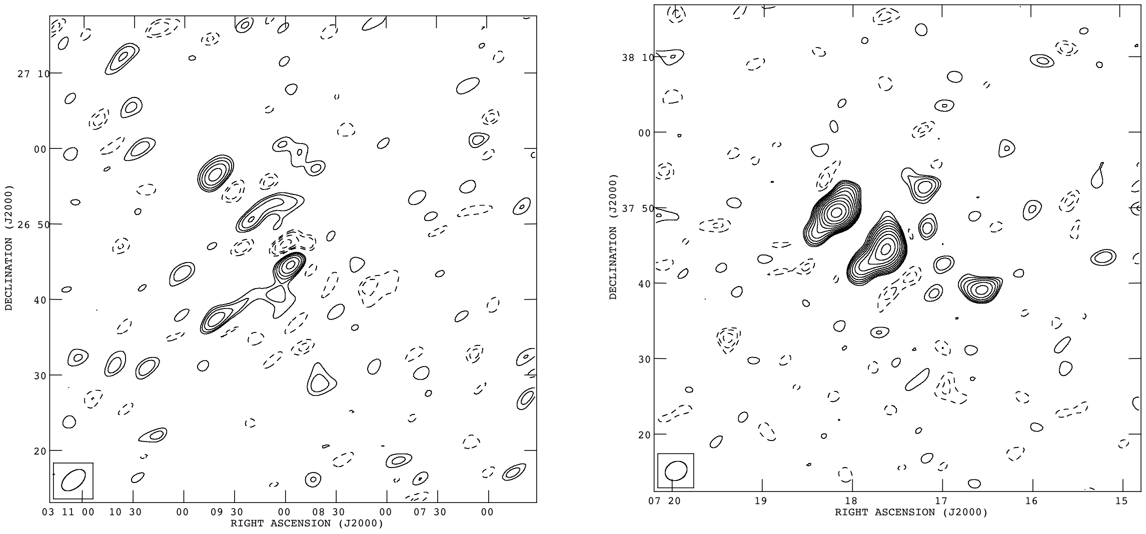

(a) MACSJ0308+26. The 1-σ map noise is 141 μJy beam^{-1}. Contour levels start at $\pm$280 μJy beam^{-1}; thereafter contours are spaced by a factor of $\sqrt{2}$.

(b) MACSJ0717+37. The 1-σ map noise is 161 μJy beam^{-1}. Contour levels start at $\pm$320 μJy beam^{-1}; thereafter contours are spaced by a factor of $\sqrt{2}$.

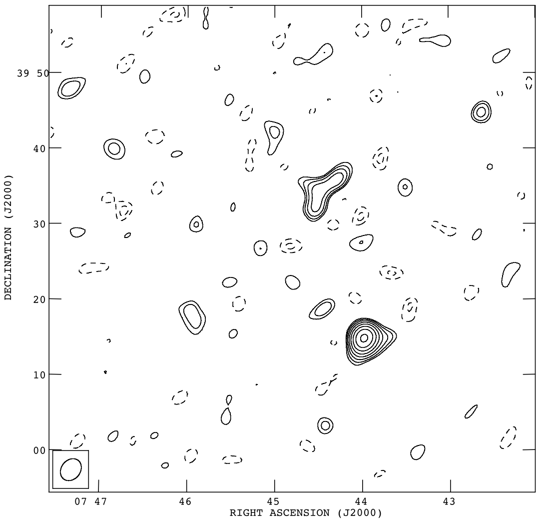

(c) MACSJ0744+39. The 1-σ map noise is 317 μJy beam^{-1}. Contour levels start at $\pm$630 μJy beam^{-1}; thereafter contours are spaced by a factor of $\sqrt{2}$.

Figure 3. SA naturally weighted, untapered, primary-beam-uncorrected maps of the MACS clusters. No source subtraction was undertaken for these images. The synthesized beam is indicated in the lower left-hand corner of each image.

at pressure p, a radius r from the cluster centre is

$$\frac{\mathrm{d}p\,(r)}{\mathrm{d}r} = -\frac{GM_r\rho\,(r)}{r^2}, \tag{2}$$

where $M_r \equiv M(<r)$ is the total mass (gas plus dark matter) internal to radius r and the gas' density distribution $\rho(r)$ is

$$\rho\,(r) = \frac{\rho\,(r=0)}{\left[1+(r/r_\mathrm{c})^2\right]^{3\beta/2}}. \tag{3}$$

The density profile has a flat top at low r/r_c (with r_c the core radius), then turns over and at large r/r_c has a logarithmic slope of -3β. The profile may be integrated to find the gas mass M_gas within r.

One also requires the equation of state of the gas, i.e. $p(\rho)$. For ideal gas, $p = \frac{\rho}{\mu}k_\mathrm{B}T$, with μ the effective mass of protons per gas particle (we take $\mu = 0.6m_\mathrm{p}$), equation (2) becomes

$$\frac{\mathrm{d}}{\mathrm{d}r}\left(\frac{\rho k_\mathrm{B}T}{\mu}\right) = -\frac{GM_r\rho}{r^2}, \tag{4}$$

and one obtains

$$M_r = -\frac{k_\mathrm{B}T}{\mu G}\frac{r^2}{\rho}\frac{\mathrm{d}\rho}{\mathrm{d}r} = \frac{3\beta r^3}{r_\mathrm{c}^2+r^2}\frac{k_\mathrm{B}T}{\mu G}. \tag{5}$$

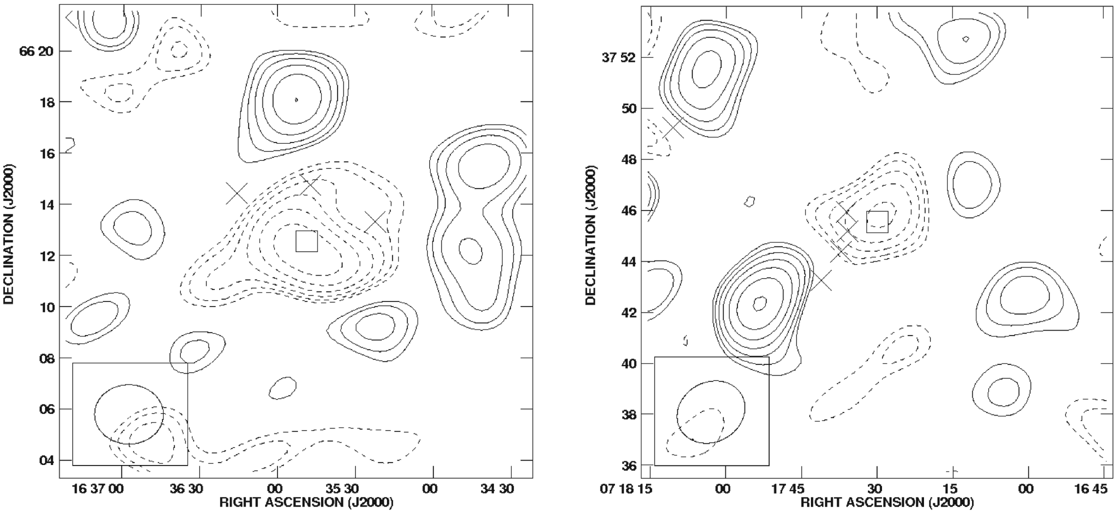

(a) A2218. The 1-σ map noise is 88 μJy beam^{-1}. Contour levels start at $\pm 180\,\mu$Jy beam^{-1}; thereafter contours are spaced by a factor of $\sqrt{2}$.

(b) MACSJ0717+37. The 1-σ map noise is 161 μJy beam^{-1}. Contour levels start at $\pm 320\,\mu$Jy beam^{-1}; thereafter contours are spaced by a factor of $\sqrt{2}$.

Figure 4. Source-subtracted SA naturally weighted, untapered, primary-beam-uncorrected maps of two clusters: A2218 and MACS J0717+37. The synthesized beam is indicated in the lower left-hand corner of each image.

Table 4. Mean flux density values for detected radio sources in the maps of A2218 and MACS J0717+37 obtained using our Bayesian analysis software. Source labels follow from Table 3. For A2218, source 6 was considered to be sufficiently far from the cluster centre to be included in our analysis.

Cluster	Source	S/mJy
A2218	1	2.7 ± 0.1
	2	1.8 ± 0.1
	3	5.7 ± 0.1
	4	2.7 ± 1.0
	5	12.7 ± 0.4
	7	6.9 ± 0.2
MACS J0717+37	1	3.0 ± 0.2
	2	2.9 ± 0.3
	3	4.4 ± 0.3
	4	2.9 ± 0.2
	5	22.0 ± 0.2
	6	5.2 ± 0.4

Table 5. Fitted parameter names and priors for the cluster analysis. The 15–22 GHz probability kernel for source spectra is α_i.

Cluster	
$\boldsymbol{x}_{\rm c}$	Gaussian, $\sigma = 1.0$ arcmin
z	δ-function
$r_{\rm c}$	Uniform, 10–1000 kpc h^{-1}
β	Uniform, 0.3–1.5
T	Gaussian, value from literature ±15 per cent
$M_{\rm gas,200}$	Uniform in log-space, (0.01–5.00) × $10^{14}{\rm M}_{\odot}\,h^{-2}$
Radio sources	
$\boldsymbol{x}_i$	δ-function
S_i	Gaussian, ±30 per cent
α_i	Smoothed version of that in Waldram et al. (2007)

4.3 Priors used here

The forms of the priors we have assumed for cluster and source parameters are given in Table 5. Positions $\boldsymbol{x}_{\rm c}$, redshifts z and gas temperatures T for individual clusters are quoted in Table 2. For the sources, positions $\boldsymbol{x}_i$ and fluxes S_i are in Table 3, and α_i is the 15–22 GHz probability kernel for source spectral index. Note that for radio sources, we use δ-functions on source positions since the position error of a source is much smaller than an SA-synthesized beam, while for source fluxes, we use a Gaussian centred on the flux density from high-resolution observations with a 1σ width of ±30 per cent to allow for variability, but for A773 we later tighten the prior on source flux (see Feroz et al. 2009, for details). We have based our spectral index prior on Waldram et al. because this contains the only measured spectral index distribution at relevant frequencies and flux densities; we would like to distinguish between field sources and sources in the clusters but have no ready means of doing so.

We now comment on our use of a single temperature for each cluster. Much SZ work so far has concentrated on the inner parts of clusters, but as one moves to radii larger than, say, r_{2500} the observational position on $T(r)$ seems to be unclear. The following examples from the literature attempt to measure $T(r)$ out to about half the classical virial radius, i.e. half of r_{180} (Peebles 1993), in samples of clusters. In 30 clusters observed with *ASCA*, Markevitch et al. (1998) find that on average T drops to about 0.6 of its central value by $0.5r_{180}$. Using *ROSAT* observations of 26 clusters, Irwin, Bregman & Evrard (1999) rule out a temperature drop of 20 per cent at 10 keV within $0.35r_{180}$ at 99 per cent confidence. With *BeppoSAX* observations of 21 clusters, De Grandi & Molendi (2002) find that on average T falls to about 0.7 of its central value by $0.5r_{180}$. With *Chandra* observations of 13 relaxed clusters, Vikhlinin et al. (2005) find that on average T falls by about 40 per cent between 0.15 and $0.5r_{180}$ but with near-flat exceptions. In *XMM–Newton* observations of 48 clusters, Leccardi & Molendi (2008) find that most have T falling by 20–40 per cent from 0.15 to $0.4r_{180}$ but that a minority are flat. Using *XMM–Newton* data on 37 clusters, Zhang et al. (2008) find that $T(r)$ is broadly flat between 0.02 and $1r_{500}$.

We have tried to find measurements in the literature of $T(r)$ out to large r for our seven clusters, with the following results. Using *Chandra* data on A611, Donnarumma et al. (2011) find that T peaks at 200 kpc and falls to 80 per cent of the peak at 600 kpc. For A773, Govoni et al. (2004) show a temperature map from *Chandra* out to 400-kpc radius with mean T about 8 keV with hotter and colder patches but no clear radial trend; Cavagnolo et al. (2009) show a radial temperature profile from *Chandra* which is consistent with being flat to 700 kpc, but it is unclear what happens further out. For A1914, Zhang et al. (2008) find from *XMM–Newton* data that $T(r)$ is flat from 150 to 900 kpc, while on the other hand, Mroczkowski et al. (2009) find from *Chandra* data that $T(r)$ falls from 9 keV at 0.2 Mpc to 6.6 keV at 1.2 Mpc. For A2218, Pratt, Böhringer & Finoguenov (2005) find from *XMM–Newton* data that $T(r)$ falls from 8 keV near the centre to 6.6 keV at 700 kpc; consistent with this is the profile in Cavagnolo et al. (2009) from *Chandra* data. Cavagnolo et al. (2009) show temperature profiles from *Chandra* data on the three MACS clusters: for 0308+26, the profile – assessed purely by eye – is probably more consistent with T falling with radius than T being independent of radius; for 0717+37, T clearly falls from 12 keV at 500 kpc to 7 keV at 1 Mpc; and for 0744+39, it is unclear what is happening.

X-ray analysis at large r is of course hampered by uncertainty in the background. The satellite *Suzaku* has a low orbit which results in some particle screening by the Earth's magnetic field and thus a low background. George et al. (2009) find that in cluster PKS0745–191, $T(r)$ falls by roughly 70 per cent from 0.3 to r_{200} with no extrapolation of the data in r and indeed going beyond r_{200}, and Bautz et al. (2009) and Hoshino et al. (2010) find somewhat similar behaviour in A1795 and A1413, respectively. As far as we know, these are as yet the only relevant X-ray observations that extend to very large r.

In view of the foregoing, we have chosen to assume isothermality (at the temperatures given in Table 2), and to examine the consequences in this case.

5 EVIDENCE

We consider two basic models as follows. The first model consists of hypothesis H_1 that the data support thermal and CMB noise plus a number of contaminating radio sources, together with priors on source parameters. The second model consists of hypothesis H_2 that the data support the two noise contributions plus the contaminating sources and also a cluster in the SZ with a β-profile, plus priors on the fitted parameters. We have carried out the analysis in two stages: first, determining the best modelling of the source contributions in each cluster field; and secondly, determining in each field the extent, if any, to which H_2 is supported over H_1.

5.1 Source model selection

Inside each of H_1 and H_2, we can consider different models for the field of contaminating sources. We now discuss the use of the Bayesian evidence for model selection in the two cases (A773 and A1914) for which source observations suggested a possible choice of source model.

5.1.1 A773

The models for A773 all include seven point sources: none was detected with the RT, two were found in the SA data and five were found with subsequent LA observations (see Table 3). We compared two models, in which the flux uncertainties were ±30 per cent, to allow for variability, and another in which the flux uncertainties were reduced to ±10 per cent. We carried out a Bayesian analysis run for the first model and another for the second. The difference in the $\log_e$-evidence was 1.20 ± 0.11, marginally favouring the 10 per cent model; that is, the odds in favour of the 10 per cent model over the 30 per cent model are 3.3 ± 1.1 to 1. There is thus little to choose between the models. For A773, we have used the 10 per cent model but kept the 30 per cent model for the other clusters.

Table 6. Relative evidences for different source models for A1914.

Model	Sources	Relative $\log_e$-evidence
A	6	5.56 ± 0.19
B	6	10.05 ± 0.17
C	7	0.0

5.1.2 A1914

For A1914, we consider three source models, all of which have one source from the SA long baselines and four sources detected with the LA. In one of the models (A) we include an RT-detected source; in a second (B), the flux for that source is taken from the LA data (which were taken much closer in time to the SA observations), and the errors are tightened; in the third model (C), a feature in the SA image which may be a source or may be a residual is also included. The relative $\log_e$-evidences for each model with respect to model C and given H_2 are shown in Table 6.

Model C, which includes the source candidate possibly detected by the SA, is overwhelmingly disfavoured relative to the two models (A and B) that have only six sources: we conclude the feature is a residual, and we discard model C.

Of the two models with six sources, model B, in which the point-source flux errors are tightened, is favoured (relative to model A) by an odds ratio of $e^{4.49 \pm 0.16}$. Consequently, we select model B as the preferred model for parameter estimation. Once again, we see that the Bayesian evidence is a useful and straightforward tool for model selection in cases where we want to test for source detection and errors on prior fluxes.

5.2 Cluster detections

For each cluster, the $\log_e$-evidence difference ΔZ for H_2 over H_1, that is, the $\log_e$-evidence for an SZ signal over and above (thermal noise plus CMB primary anisotropies plus the radio sources we have considered) for each cluster model are shown in Table 7. Thus the formal evidence ratios, given by $E = \exp \Delta Z$, are huge (ranging from 10^{11} to 10^{43}) except for MACS J0744+39. For this cluster, E is about 3000, i.e. there is a one in 3000 chance that the SZ detection is spurious; note that this is the cluster for which the thermal noise is at least twice that of any of the others. Of course, we know from optical and/or X-ray that a cluster is present in each case. Thus the high E-values indicate the power of the observing plus analysis methodology for detecting SZ even in the presence of serious source confusion. The methodology works even with substantial uncertainty on the source fluxes but requires that the existences of the sources, in approximately the right positions, are correctly determined. Of course, the methodology and its resultant

Table 7. For each cluster, the $\log_e$-evidence ΔZ for an SZ signal in addition to thermal noise plus CMB primary anisotropies plus the n sources.

Cluster	n	ΔZ
A611	2	27.27 ± 0.12
A773	7	27.13 ± 0.09
A1914	6	64.84 ± 0.11
A2218	7	92.26 ± 0.23
MACS J0308+26	3	47.59 ± 0.13
MACS J0717+37	6	33.90 ± 0.19
MACS J0744+39	4	7.88 ± 0.16

evidence ratios cannot take into account errors arising from causes that are not modelled.

6 SOURCE SUBTRACTION

For this subsection only, we return to the source-subtracted maps. For our two worst case examples (see Section 3.1), of Abell 2218 and MACS J0717+37, the source-subtracted SA maps are shown in Fig. 4 but this time using the source flux density values from our Bayesian analyses (the positions are still from Table 3) which must help overcome the effects of some variability.

The subtracted maps show significant radio source emission that we have not subtracted in these maps. One can assess the contribution to a false SZ 'detection' by centring the SZ-map CLEAN beam (Fig. 5a) over each source and estimating the beam's sidelobe at the position of the cluster. For example, in A2218, the brightest unsubtracted source at 16 35 50 + 66 18 has a flux density of 1.02 mJy, and Fig. 5(b) indicates a contribution over the cluster of some −5 per cent, i.e. some −50 μJy. This is negligible compared to the measured SZ flux density peak of −1.35 mJy. In MACS J0717+37, the most relevant source is at 07 17 53 + 37 42, which has a peak of 2.54 mJy, and the CLEAN beam indicates a contribution over the cluster of some −3 per cent, i.e. some −80 μJy, again negligible compared with the SZ peak of −1.38 mJy.

For MACS J0717+37, one must also consider whether the steep-spectrum radio halo (see in particular van Weeren et al. 2009) might be contaminating our SZ map. In fact, we do not think the halo can cause significant contamination for the following reasons. First, the deep (given observing frequencies) images at 0.6, 1.4 and 5.0 GHz in van Weeren et al. show no emission west of 07 17 30, whereas the centre of the AMI SZ decrement is at 07 17 30 +37 46; the halo emission in van Weeren et al. east of 07 17 30 has a spectral index α (in their paper flux density $\propto$ frequency$^{-\alpha}$) fitted over 0.6, 1.4 and 5.0 GHz of <-1 so that α at >10 GHz will be far steeper, and it is hard to see how AMI can detect this emission at 16 GHz. Secondly, to overcome the problem that the RT observations have little sensitivity to sources bigger than the RT beam, we have maximized sensitivity to extended sources (such as a halo) whilst minimizing contamination from SZ by making higher resolution SA maps with uv-minima of 500 and 700: these show emission associated with R1, HT and FR 1 in fig. 2 of van Weeren et al. which they find at 8.5 GHz, but show nothing of any halo to the west in the direction of the cluster.

7 PARAMETER ESTIMATES AND DISCUSSION

The full posterior probability distributions for the seven clusters are shown in Figs 6–12. In each figure, the upper panel shows the posterior distributions for the fitted parameters, marginalized into two dimensions, and into one dimension along the diagonal; the lower panel shows the 1D marginalized posterior distributions for parameters derived from those that were fitted. In Table 8, we give mean (and limits at 68 per cent confidence) a posteriori parameter estimates for the clusters, but we emphasize that these can mislead: there is no substitute for looking at the probability distributions.

There are two technical points to be aware of. First, some of the distributions have rough sections. This roughness is just the noise due to the finite numbers of samples. We have used narrow binning of parameter values to avoid misleading effects of averaging, especially at distribution edges, with the consequence of high noise per bin. Secondly, there is a possibility that, for some combination of cluster parameters, nowhere in the cluster does the density reach $a \times \rho_{\rm crit}$, resulting in no physical solution for r_a. We set r_a to zero in such cases. Of the seven clusters analysed in this paper, this affected only MACS J0744+39, resulting in a sharp peak in the posterior probability of r_{1000}/h^{-1} Mpc and r_{500}/h^{-1} Mpc close to zero

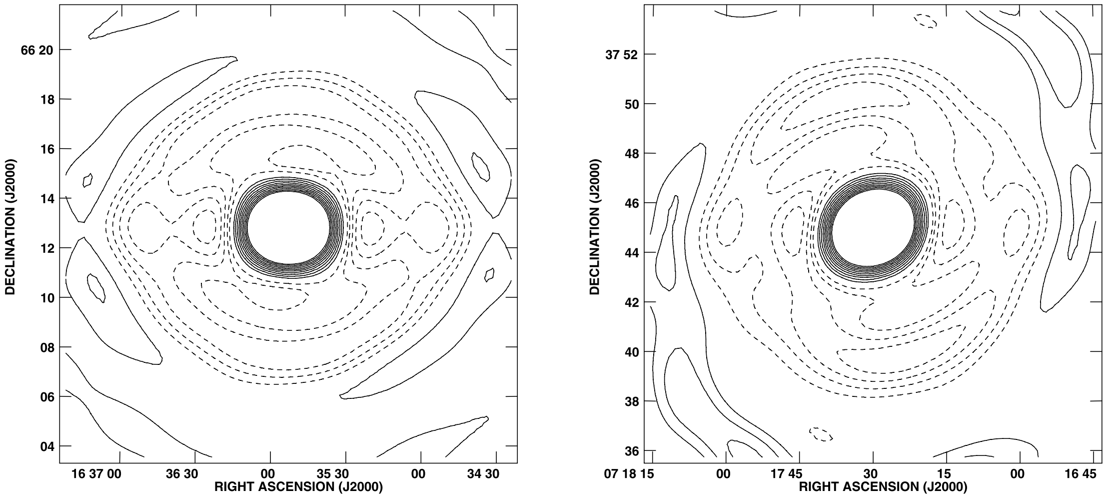

(a) A2218.

(b) MACSJ0717+37.

Figure 5. Synthesized beams for A2218 and MACS J0717+37. Contour levels begin at 3 per cent and increase by 3 per cent thereafter.

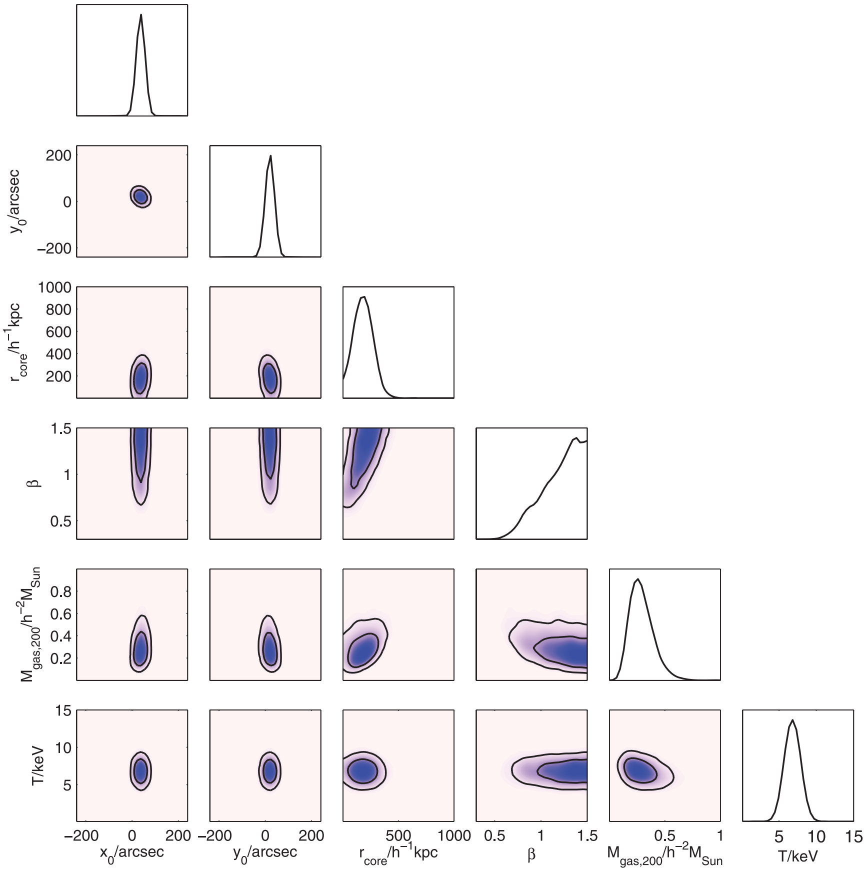

(a) For fitted parameters, posteriors marginalized into two dimensions, and into one dimension along the diagonal.

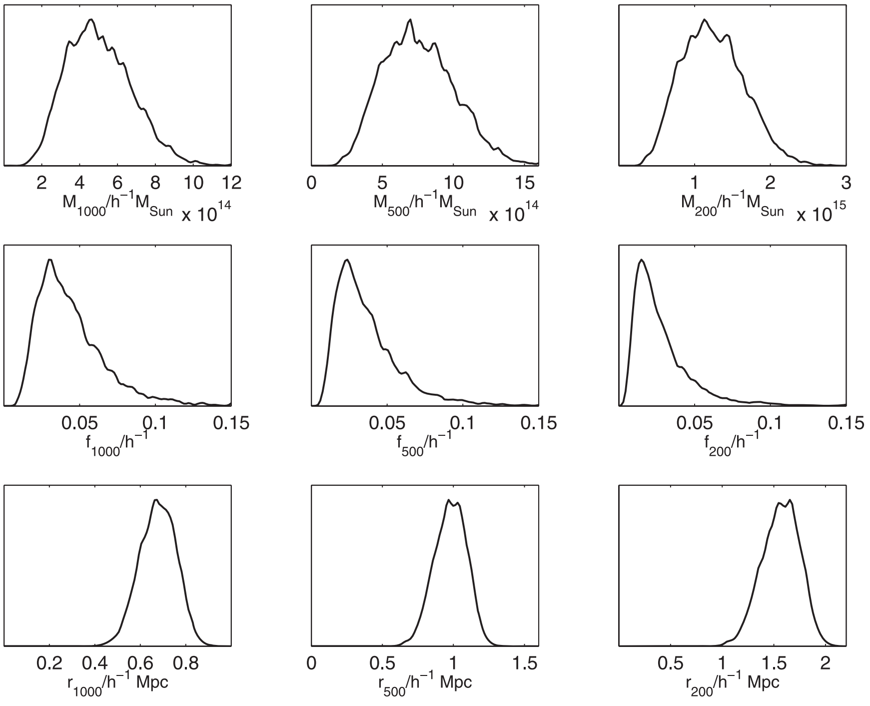

(b)

Figure 6. A611 posterior probability distribution.

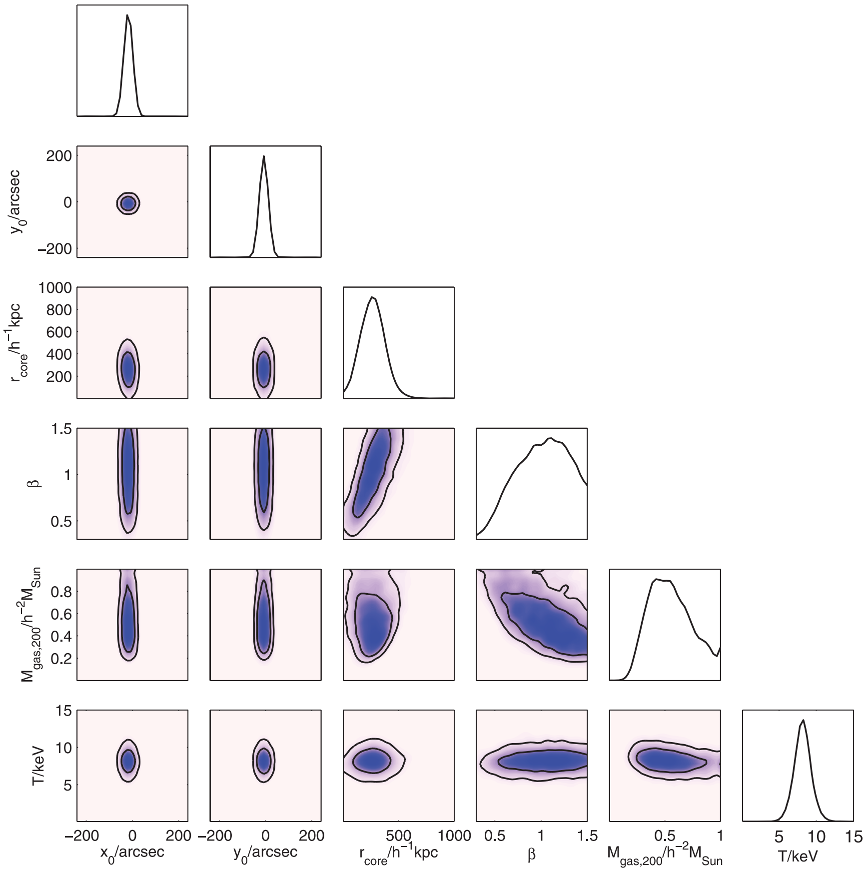

(a) For fitted parameters, posteriors marginalized into two dimensions, and into one dimension along the diagonal.

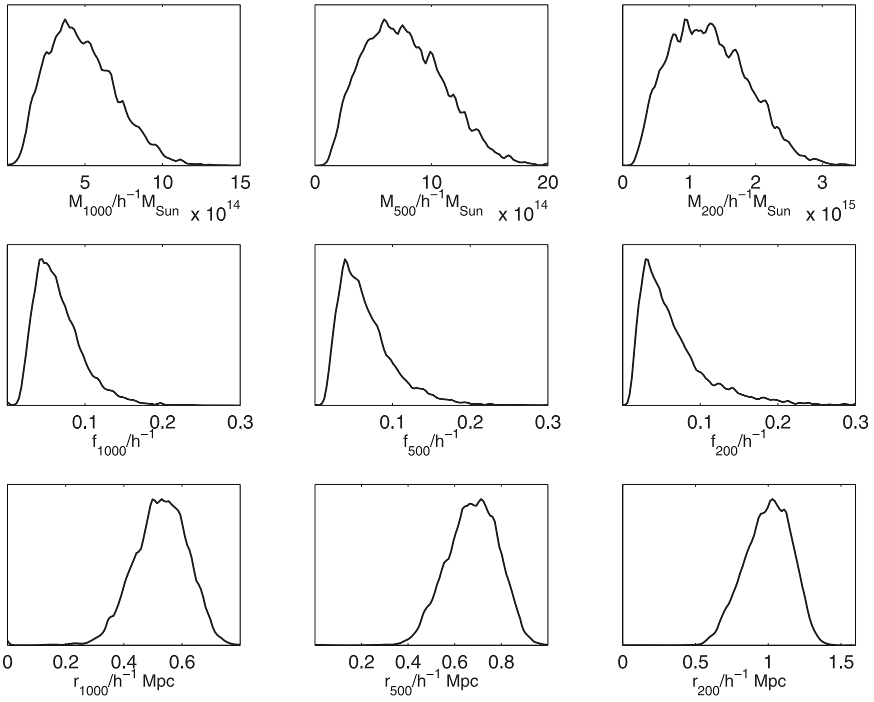

(b) For derived parameters, posteriors marginalized into one dimension.

Figure 7. A773 posterior probability distribution.

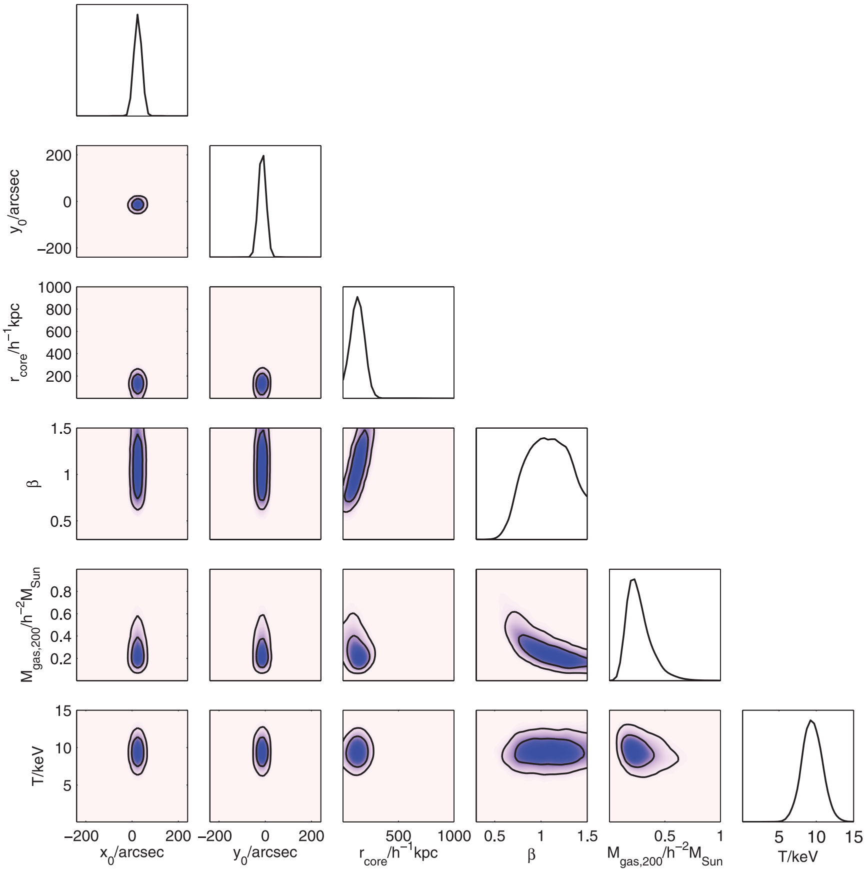

(a) For fitted parameters, posteriors marginalized into two dimensions, and into one dimension along the diagonal.

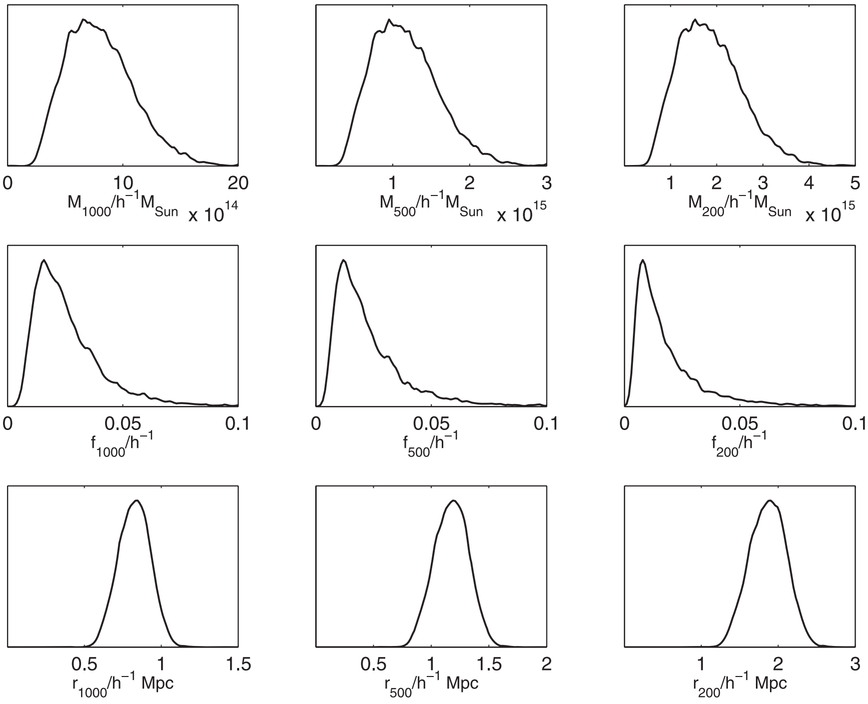

(b) For derived parameters, posteriors marginalized into one dimension.

Figure 8. A1914 posterior probability distribution.

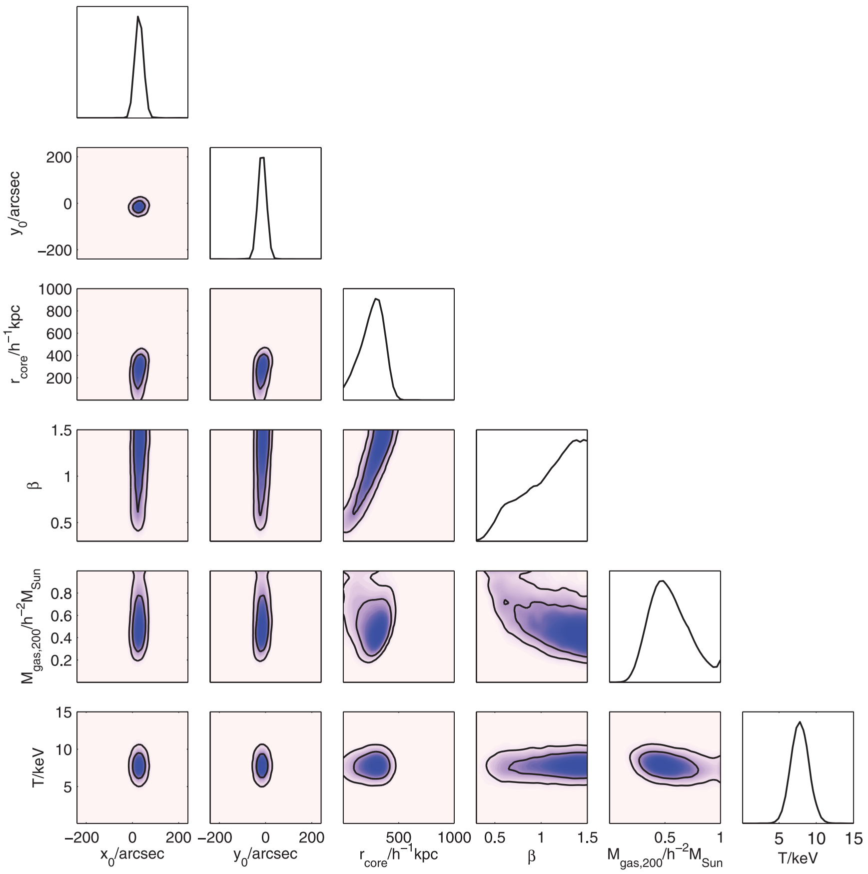

(a) For fitted parameters, posteriors marginalized into two dimensions, and into one dimension along the diagonal.

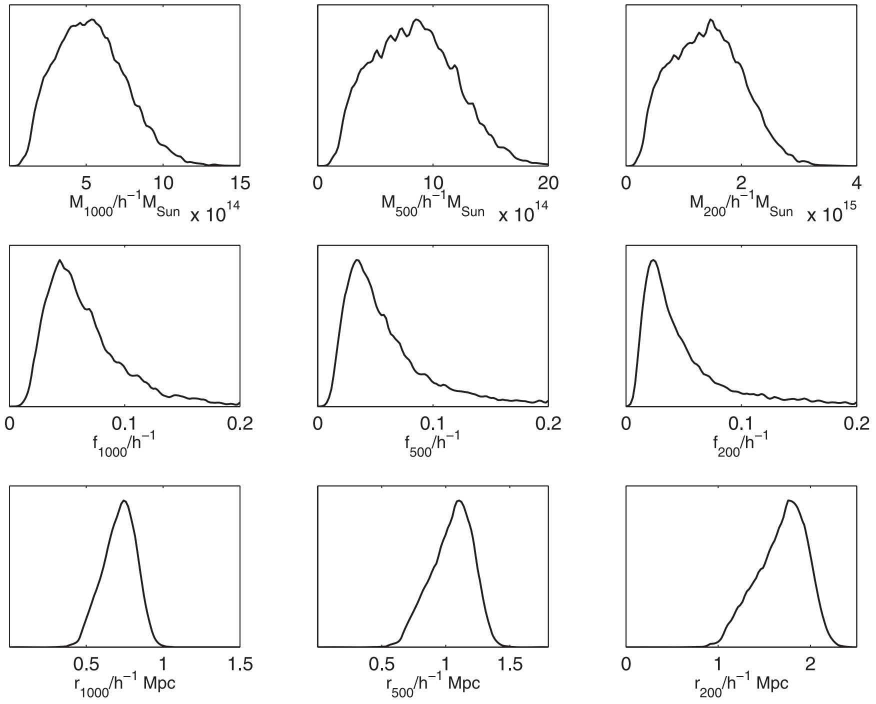

(b) For derived parameters, posteriors marginalized into one dimension.

Figure 9. A2218 posterior probability distribution.

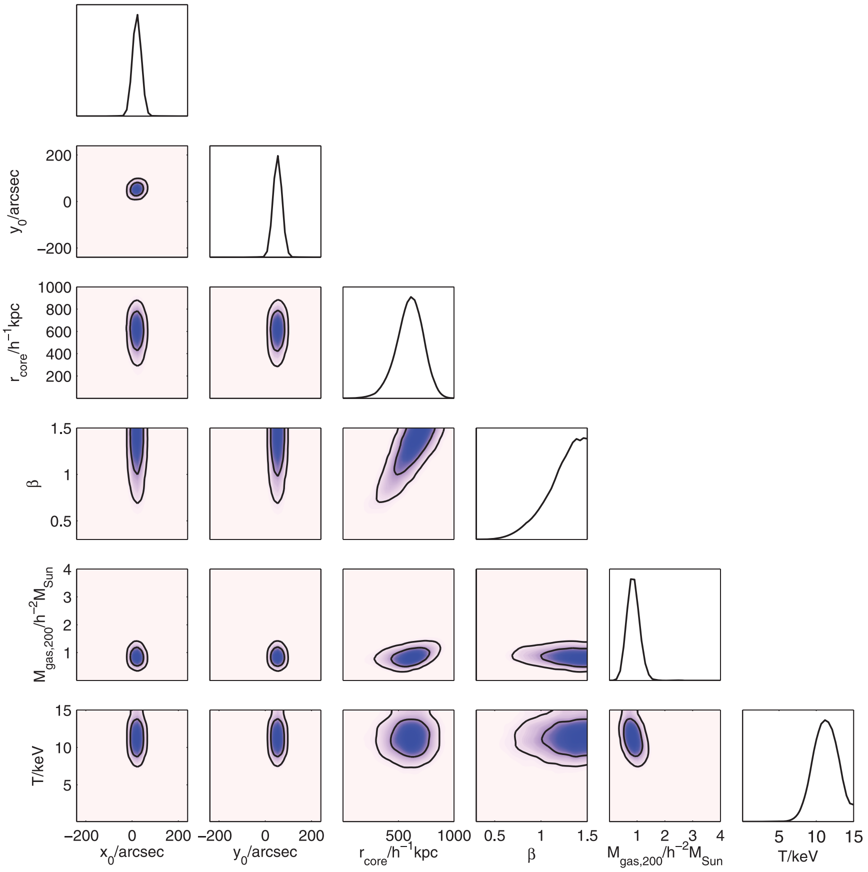

(a) For fitted parameters, posteriors marginalized into two dimensions, and into one dimension along the diagonal.

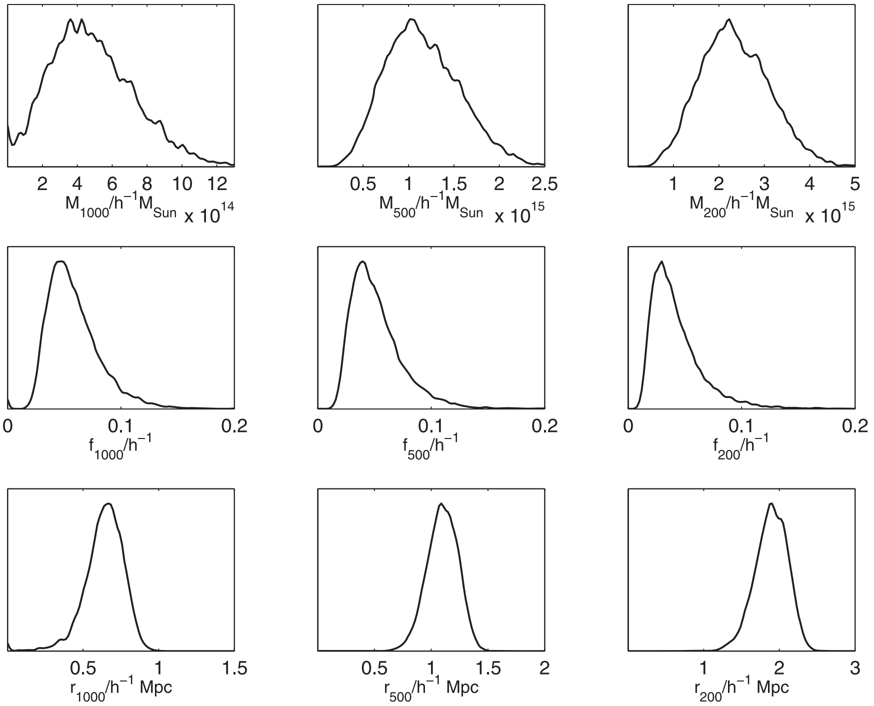

(b) For derived parameters, posteriors marginalized into one dimension.

Figure 10. MACS J0308+26 posterior probability distribution.

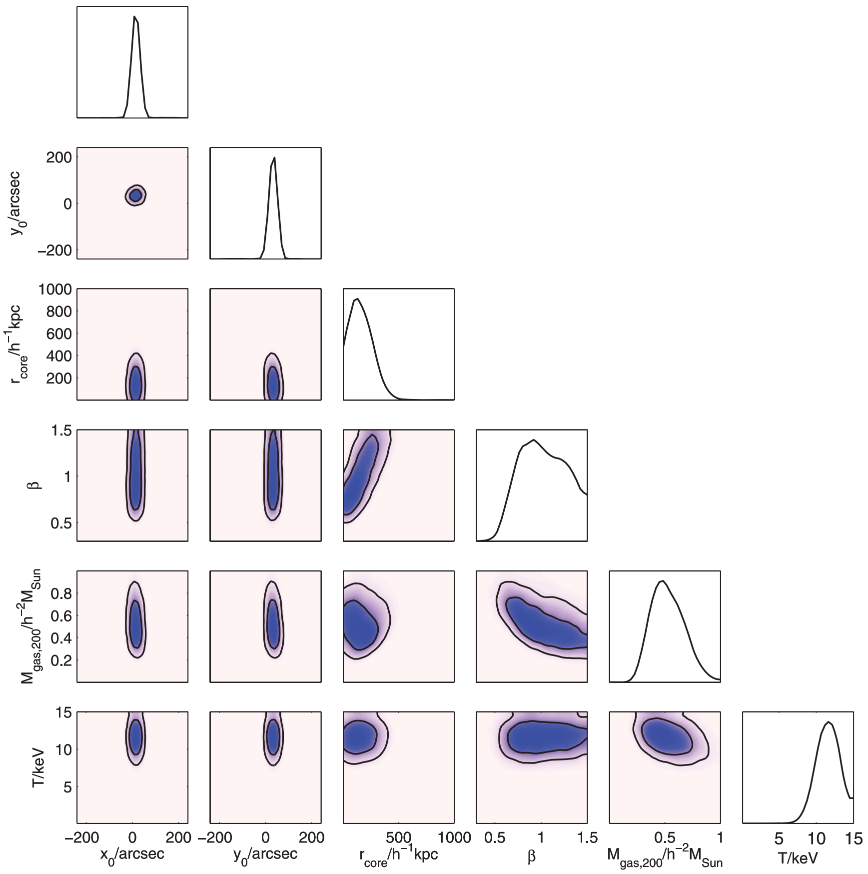

(a) For fitted parameters, posteriors marginalized into two dimensions, and into one dimension along the diagonal.

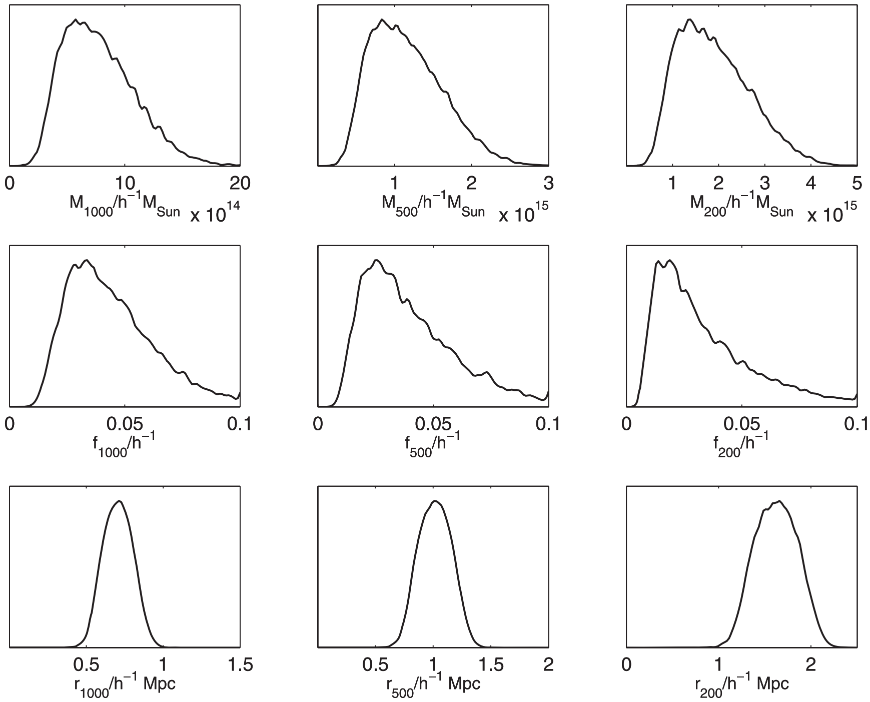

(b) For derived parameters, posteriors marginalized into one dimension.

Figure 11. MACS J0717+37 posterior probability distribution.

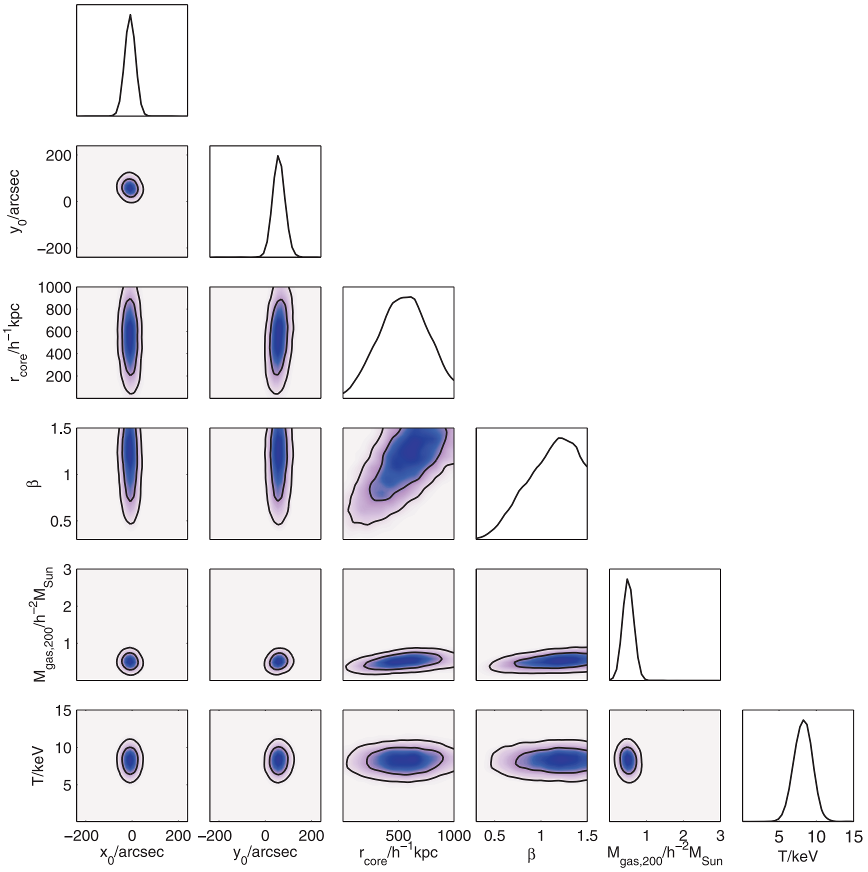

(a) For fitted parameters, posteriors marginalized into two dimensions, and into one dimension along the diagonal.

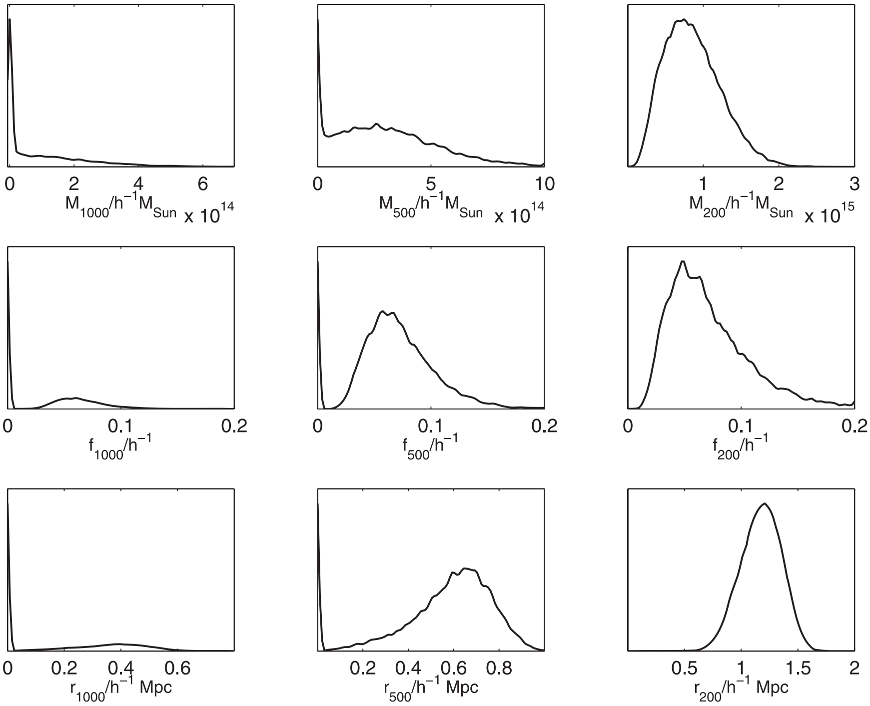

(b) For derived parameters, posteriors marginalized into one dimension.

Figure 12. MACS J0744+39 posterior probability distribution.

Table 8. Mean a posteriori parameter estimates (assuming $h = 0.70$) with 68 per cent confidence limits. The values in this table assume $h = 0.70$.

	A611	A773	A1914	A2218
r_{c} (kpc)	260^{+54}_{-60}	380^{+150}_{-150}	190^{+36}_{-39}	370^{+82}_{-58}
β	$1.2^{+0.29}_{-0.082}$	$1.0^{+0.49}_{-0.14}$	$1.1^{+0.43}_{-0.12}$	$1.1^{+0.41}_{-0.13}$
$M_{\mathrm{gas},200}$ (10^{13} M$_{\odot}$)	$6.0^{+0.71}_{-1.2}$	$12^{+1.6}_{-2.7}$	$5.5^{+0.53}_{-1.3}$	$11^{+1.3}_{-2.2}$
M_{1000} (10^{14} M$_{\odot}$)	$7.2^{+1.0}_{-1.3}$	$6.9^{+1.3}_{-1.8}$	$12^{+1.7}_{-2.3}$	$7.6^{+1.4}_{-1.8}$
M_{500} (10^{14} M$_{\odot}$)	$11^{+1.6}_{-2.0}$	$11^{+2.1}_{-2.8}$	$17^{+2.5}_{-3.5}$	$12^{+2.4}_{-2.8}$
M_{200} (10^{14} M$_{\odot}$)	$18^{+2.7}_{-3.2}$	$19^{+3.7}_{-4.8}$	$27^{+4.0}_{-5.6}$	$20^{+4.2}_{-4.8}$
r_{1000} (Mpc)	$0.68^{+0.041}_{-0.037}$	$0.53^{+0.047}_{-0.039}$	$0.83^{+0.051}_{-0.049}$	$0.71^{+0.057}_{-0.047}$
r_{500} (Mpc)	$0.98^{+0.059}_{-0.052}$	$0.68^{+0.057}_{-0.049}$	$1.2^{+0.074}_{-0.071}$	$1.0^{+0.089}_{-0.067}$
r_{200} (Mpc)	$1.6^{+0.096}_{-0.081}$	$1.0^{+0.086}_{-0.071}$	$1.9^{+0.12}_{-0.11}$	$1.7^{+0.15}_{-0.11}$
f_{1000}	$0.064^{+0.0075}_{-0.019}$	$0.095^{+0.012}_{-0.026}$	$0.038^{+0.0041}_{-0.013}$	$0.095^{+0.0095}_{-0.030}$
f_{500}	$0.053^{+0.0057}_{-0.018}$	$0.095^{+0.012}_{-0.031}$	$0.033^{+0.0028}_{-0.013}$	$0.089^{+0.0052}_{-0.036}$
f_{200}	$0.041^{+0.0028}_{-0.017}$	$0.095^{+0.0085}_{-0.040}$	$0.027^{+0.0012}_{-0.013}$	$0.083^{+0.0043}_{-0.044}$
	MACS J0308+26	MACS J0717+37	MACS J0744+39	
r_{c} (kpc)	860^{+83}_{-67}	240^{+57}_{-83}	780^{+150}_{-150}	
β	$1.2^{+0.26}_{-0.062}$	$1.0^{+0.48}_{-0.14}$	$1.1^{+0.40}_{-0.11}$	
$M_{\mathrm{gas},200}$ (10^{13} M$_{\odot}$)	$18^{+1.6}_{-2.0}$	$11^{+1.3}_{-1.7}$	$10^{+1.1}_{-1.2}$	
M_{1000} (10^{14} M$_{\odot}$)	$7.0^{+1.4}_{-7.0}$	$11^{+1.7}_{-2.6}$	$1.3^{+1.8}_{-1.3}$	
M_{500} (10^{14} M$_{\odot}$)	$17^{+2.4}_{-3.2}$	$17^{+2.7}_{-4.1}$	$4.4^{+1.2}_{-4.4}$	
M_{200} (10^{14} M$_{\odot}$)	$34^{+4.9}_{-5.6}$	$27^{+4.5}_{-6.8}$	$12^{+2.1}_{-3.0}$	
r_{1000} (Mpc)	$0.64^{+0.064}_{-0.044}$	$0.71^{+0.048}_{-0.049}$	$0.21^{+0.15}_{-0.21}$	
r_{500} (Mpc)	$1.1^{+0.068}_{-0.060}$	$1.0^{+0.072}_{-0.073}$	$0.57^{+0.11}_{-0.57}$	
r_{200} (Mpc)	$1.9^{+0.11}_{-0.090}$	$1.6^{+0.12}_{-0.12}$	$1.2^{+0.092}_{-0.081}$	
f_{1000}	$0.084^{+0.0092}_{-0.019}$	$0.065^{+0.0084}_{-0.018}$	$0.055^{+0.030}_{-0.055}$	
f_{500}	$0.075^{+0.0078}_{-0.019}$	$0.059^{+0.0079}_{-0.020}$	$0.10^{+0.016}_{-0.10}$	
f_{200}	$0.061^{+0.0058}_{-0.019}$	$0.052^{+0.0058}_{-0.022}$	$0.10^{+0.013}_{-0.032}$	

radius. Consequently, the posterior probability also peaks close to zero for derived parameters f_{1000}/h^{-1}, f_{500}/h^{-1}, M_{1000}/h^{-1} M$_{\odot}$ and M_{500}/h^{-1} M$_{\odot}$, for this cluster. A different SA configuration or more integration would help for MACS J0744+39, but at mean overdensity 200, there is no issue.

To set these results in context, we give examples from the literature of other estimates of some of these quantities that we can find for these clusters.

For A611, Schmidt & Allen (2007) using *Chandra* find a total virial mass of $6.2^{+3.8}_{-1.8} \times 10^{14}$ M$_{\odot}$. From gravitational lensing, Romano et al. (2010) find r_{200} is some 1.5 Mpc and total mass is some 4–7 × 10^{14} M$_{\odot}$. We find $M_{200} \approx 1.8 \pm 0.3 \times 10^{15}M_{\odot}$ and $r_{200} \approx 1.6 \pm 0.1$ Mpc.

For A773, Zhang et al. (2008) find from *XMM–Newton* that r_{500} is 1.3 Mpc, M_{500} is $8.3 \pm 2.5 \times 10^{14}$ M$_{\odot}$ and $f_{\mathrm{g},500}$ is 0.13 ± 0.07, while Barrena et al. (2007) estimate a virial mass of 1.2–2.7 × 10^{15} M$_{\odot}$ from *Chandra* and optical spectral velocities. We find $M_{500} \approx 1.1^{+0.2}_{-0.3} \times 10^{15}M_{\odot}$, $M_{200} \approx 1.9^{+0.4}_{-0.5} \times 10^{15}M_{\odot}$, $r_{500} \approx 6.8^{+0.6}_{-0.5} \times 10^{-1}$ Mpc and $f_{\mathrm{g},500} \approx 0.10^{+0.01}_{-0.03}$.

For A1914, Zhang et al. (2008) find from *XMM–Newton* that r_{500} is 1.7 Mpc, M_{500} is $16.8 \pm 4.9 \times 10^{14}$ M$_{\odot}$ and $f_{\mathrm{g},500}$ is 0.07 ± 0.04. Mroczkowski et al. (2009) fit jointly to *Chandra* and SZA data and find that r_{200} is 1.3 Mpc, M_{500} is 6.6–8.1 × 10^{14} M$_{\odot}$ and $f_{\mathrm{g},500}$ is 0.14–0.16, the exact values depending on assumptions, with random errors in addition. Zhang et al. (2010) find from *XMM–Newton* that M_{1000} is $4.36 \pm 1.22 \times 10^{14}$ M$_{\odot}$ and M_{500} is $7.69 \pm 2.24 \times 10^{14}$ M$_{\odot}$, while from weak lensing they find that M_{1000} is $3.35^{+0.50}_{-0.47} \times 10^{14}$ M$_{\odot}$ and M_{500} is $4.46^{+0.75}_{-0.69} \times 10^{14}$ M$_{\odot}$. We find $M_{1000} \approx 1.2{\pm}0.2 \times 10^{15}M_{\odot}$, $M_{500} \approx 1.7^{+0.3}_{-0.4} \times 10^{15}M_{\odot}$, $f_{\mathrm{g},500} \approx 0.033^{+0.003}_{-0.012}$ and $r_{200} \approx 1.9 \pm 0.1$ Mpc.

For A2218, Zhang et al. (2008) find from *XMM–Newton* that r_{500} is 1.1 Mpc, M_{500} is $4.2 \pm 1.3 \times 10^{14}$ M$_{\odot}$ and $f_{\mathrm{g},500}$ is 0.15 ± 0.09. We find $M_{500} \approx 1.2^{+0.2}_{-0.3} \times 10^{15}M_{\odot}$, $r_{500} \approx 1.0 \pm 0.1$ Mpc and $f_{\mathrm{g},500} \approx 0.089^{+0.005}_{-0.004}$.

For MACS J0744+39, Ettori et al. (2009) find from *Chandra* that r_{200} is 1566 ± 56 kpc, and also from *Chandra*, Schmidt & Allen (2007) find a virial mass of $7.4^{+4.4}_{-2.1} \times 10^{14}$ M$_{\odot}$. We find $M_{200} \approx 1.2^{+0.2}_{-0.3} \times 10^{15}M_{\odot}$ and $r_{200} \approx 1.2 \pm 0.1$ Mpc.

Returning to our results, four points are immediately apparent: our total mass estimates seem high; the gas fractions are low and get lower as r increases; as well as the usual $\beta - r_{\mathrm{c}}$ degeneracy (Grego et al. 2001; Grainge et al. 2002; Saunders et al. 2003), there is a tendency to high β; and the results go out to larger radius than typically obtained from X-ray or SZ cluster analyses. We next consider these points in more detail.

7.1 Masses and gas fractions

Rather than rising towards a canonical large-scale gas fraction of, say, 0.12 as one goes to large r (see e.g. McCarthy, Bower & Balogh 2007; Komatsu et al. 2009; Ettori et al. 2009), our f_{g} values are low and get smaller as r increases. We suspect that our assumption of isothermality may be the cause. If, away from the central region, $T(r)$ keeps falling as r increases, then of course our isothermal assumption is invalid. The consequences of this for estimating M and f_g are, however, somewhat worse than we initially expected for the following reason. In the literature, it is assumed that the value for M_r based on hydrostatic equilibrium (equation 5 in this work) implies $M_r \propto T$. However, one has to use equation (5) in terms of radius r_a internal to which there is a specific mean overdensity a. At a particular r_a, one can equate M_r from equation (5) with the expression for M_r from integrating over spherical shells, finding that $r_a \propto T^{1/2}$ and in fact $M_r \propto T^{3/2}$ (please note our stated convention at the end of Section 1). Since $M_{\mathrm{gas},r} \propto T^{-1}$ (given the SZ measurement), $f_{\mathrm{gas},r}$ is proportional to $T^{-5/2}$ rather than the T^{-2} in the literature. It is not possible here to make an approximate quantitative estimate of the effects of the isothermal assumption because of its separate effects on r_c, on β and on total and gas masses as functions of r. Nevertheless, if temperatures are less than what we have assumed, our total mass estimates are biased high, our gas fraction estimates are biased low and our r_a estimates are somewhat biased high.

7.2 Reaching the virial radius

Lacey & Cole (1993) give an expression for how the classical virial radius (r_{178} at $z = 0$) changes with z in an $\Omega - \Lambda$ universe: for our lowest and highest cluster redshifts, the virial radii are approximately r_{205} and r_{215}. The SA's sensitivity to structures out to diameters of 10 arcmin corresponds to sensitivity to a physical diameter of 1.7 Mpc at our lowest cluster redshift. Given that our r_{200} estimate is biased high, our plots at overdensity 200 thus reach the virial radius in our nearer clusters with some extrapolation of the SZ signal and with no extrapolation (but still necessarily some interpolation) in the more distant ones.

7.3 β

Typical low-r β-values are about 0.7 (see e.g. Jones & Forman 1984; Mohr, Mathiesen & Evrard 1999; Ettori et al. 2004) and reach about 0.9 by r_{1000} (see e.g. Vikhlinin, Forman & Jones 1999; Hallman et al. 2007). Despite the β–r_c degeneracy, when we marginalize over everything but β, we find that β is much larger. There are two likely reasons for this. First, our data go to larger angular scale than is almost always the case in the literature. Secondly, if T indeed falls as r increases, then the estimate of $M_{\mathrm{gas},r}$ will fall as r increases given that T is assumed independent of r. At present, we cannot assess the relative contributions of these two factors.

8 CONCLUSIONS

(i) Untapered, naturally weighted AMI SA maps at 13.9–18.2 GHz, with no source subtraction, show clear SZ effects in five of the seven clusters.

(ii) Using source-subtraction observations, about half of which are from the RT (and thus at 15 GHz but typically 2 years before the SA observations), and assuming a spherical β-model, hydrostatic equilibrium and isothermality with an X-ray-measured temperature, our Bayesian analysis reveals SZ signals in all seven clusters. In six of these, the formal Bayesian evidence for an SZ detection, in addition to sources plus CMB primary anisotropies plus thermal noise, is huge; in one of them with much the worst thermal noise, there is a one in 3000 chance that the SZ is spurious. We emphasize that to allow for variability, we set the prior on each source's flux density as its high-resolution value with a Gaussian 1σ width of (except in the case of A773) ±30 per cent.

(iii) The Bayesian evidence proves very useful in understanding source environments. For example, a high-resolution map showed a feature that, by eye, was classed as a tentative radio source detection. Running the Bayesian analysis twice, with and without that tentative source, showed that the evidence for it is in fact so low that it should not be included.

(iv) We note that our sensitivity to structures out to 10 arcmin, corresponding to a 1.7-Mpc diameter for our lowest redshift cluster, means that our parameter estimates out to the classical virial radii of the nearer clusters involve some extrapolation, but no extrapolation (but still necessarily some interpolation) is needed for the more distant ones.

(v) Our probability distributions of masses and radii internal to which the average overdensities are 1000, 500 and 200 are usefully constrained and change sensibly over this range. *However*, our gas fractions are evidently low compared with values in the literature; further, they decrease with increasing radius, which is also unexpected. The problem seems consistent with the notion that temperature T decreases as radius r increases whereas we are assuming isothermality (using temperatures measured from low-radii data); the problem is made somewhat worse because, as we have shown, gas fraction goes as $T^{-2.5}$ assuming isothermality and hydrostatic equilibrium rather than as T^{-2} as seems to have been assumed in the literature. If T does indeed fall as r increases, our gas masses are biased low and our total masses (and to a lesser extent our measurements of r_a) are biased high. Temperature profiles must be measured or some other means found to deal with this problem if we are to infer masses out towards the virial radius. Indeed, along with other density profile models, this will be investigated in future work.

ACKNOWLEDGMENTS

We thank PPARC/STFC for support for AMI and its operation. We thank PPARC for support for the RT and its operation. We warmly acknowledge the staff of Lord's Bridge and of the Cavendish Laboratory for their work on AMI and the RT. MLD, TMOF, MO, CR-G and TWS acknowledge PPARC/STFC studentships. The analysis work was conducted in cooperation with SGI/Intel using the Altix 3700 supercomputer at DAMTP, University of Cambridge supported by HEFCE and STFC, and we are grateful to Andrey Kaliazin for computing assistance. We thank the anonymous referee for very useful comments and suggestions.

REFERENCES

AMI Collaboration: Barker R. et al., 2006, MNRAS, 369, L1
AMI Consortium: Franzen T. M. O. et al., 2009, MNRAS, 400, 995
AMI Consortium: Hurley-Walker N. et al., 2009a, MNRAS, 396, 365
AMI Consortium: Hurley-Walker N. et al., 2009b, MNRAS, 398, 249
AMI Collaboration: Hurley-Walker N. et al., 2011, MNRAS, submitted, arXiv:1101.5912
AMI Collaboration: Rodriguez-Gonzalvez C. et al., 2011a, MNRAS, submitted, arXiv:1101.5589
AMI Collaboration: Rodriguez-Gonzalvez C. et al., 2011b, MNRAS, 414, 3751
AMI Consortium: Scaife A. M. M. et al., 2008, MNRAS, 385, 809
AMI Consortium: Scaife A. M. M. et al., 2009a, MNRAS, 394, L46
AMI Consortium: Scaife A. M. M. et al., 2009b, MNRAS, 400, 1394
AMI Consortium: Shimwell T. W., 2011, MNRAS, submitted, arXiv:1101.5590
AMI Consortium: Zwart J. T. L. et al., 2008, MNRAS, 391, 1545

Balestra I., Tozzi P., Ettori S., Rosati P., Borgani S., Mainieri V., Norman C., Viola M., 2007, A&A, 462, 429

Barrena R., Boschin W., Girardi M., Spolaor M., 2007, A&A, 467, 37

Bautz M. W. et al., 2009, PASJ, 61, 1117

Birkinshaw M., 1999, Phys. Rep., 310, 97

Birkinshaw M., Hughes J. P., 1994, ApJ, 420, 33

Böhringer H. et al., 2000, ApJS, 129, 435

Bolton R. C., Chandler C. J., Cotter G., Pearson T. J., Pooley G. G., Readhead A. C. S., Riley J. M., Waldram E. M., 2006, MNRAS, 370, 1556

Bonamente M., Joy M. K., Carlstrom J. E., Reese E. D., LaRoque S. J., 2004, ApJ, 614, 56

Carlstrom J. E., Joy M., Grego L., 1996, ApJ, 456, L75

Carlstrom J. E., Holder G. P., Reese E. D., 2002, ARA&A, 40, 643

Carlstrom J. E. et al., 2011, PASP, 123, 568

Cavagnolo K. W., Donahue M., Voit G. M., Sun M., 2009, VizieR Online Data Catalog, 218, 20012

Condon J. J., Cotton W. D., Greisen E. W., Yin Q. F., Perley R. A., Taylor G. B., Broderick J. J., 1998, AJ, 115, 1693

De Grandi S., Molendi S., 2002, ApJ, 567, 163

Dobbs M. et al., 2006, New Astron. Rev., 50, 960

Donnarumma A. et al., 2011, A&A, 528, A73

Ebeling H., Edge A. C., Henry J. P., 2001, ApJ, 553, 668

Ebeling H., Barrett E., Donovan D., 2004, ApJ, 609, L49

Ebeling H., Barrett E., Donovan D., Ma C.-J., Edge A. C., van Speybroeck L., 2007, ApJ, 661, L33

Ebeling H., Edge A. C., Mantz A., Barrett E., Henry J. P., Ma C. J., van Speybroeck L., 2010, MNRAS, 407, 83

Edge A. C., Ebeling H., Bremer M., Röttgering H., van Haarlem M. P., Rengelink R., Courtney N. J. D., 2003, MNRAS, 339, 913

Ettori S., Tozzi P., Borgani S., Rosati P., 2004, A&A, 417, 13

Ettori S., Morandi A., Tozzi P., Balestra I., Borgani S., Rosati P., Lovisari L., Terenziani F., 2009, A&A, 501, 61

Feroz F., Hobson M. P., 2008, MNRAS, 384, 449

Feroz F., Hobson M. P., Zwart J. T. L., Saunders R. D. E., Grainge K. J. B., 2009, MNRAS, 398, 2049

George M. R., Fabian A. C., Sanders J. S., Young A. J., Russell H. R., 2009, MNRAS, 395, 657

Govoni F., Markevitch M., Vikhlinin A., van Speybroeck L., Feretti L., Giovannini G., 2004, ApJ, 605, 695

Grainge K., Jones M., Pooley G., Saunders R., Baker J., Haynes T., Edge A., 1996, MNRAS, 278, L17

Grainge K., Jones M. E., Pooley G., Saunders R., Edge A., Grainger W. F., Kneissl R., 2002, MNRAS, 333, 318

Grainger W. F., Das R., Grainge K., Jones M. E., Kneissl R., Pooley G. G., Saunders R. D. E., 2002, MNRAS, 337, 1207

Grego L., Carlstrom J. E., Reese E. D., Holder G. P., Holzapfel W. L., Joy M. K., Mohr J. J., Patel S., 2001, ApJ, 552, 2

Hallman E. J., Burns J. O., Motl P. M., Norman M. L., 2007, ApJ, 665, 911

Hand N. et al., 2011, ApJ, 731, 39

Hincks A. D. et al., 2010, ApJS, 191, 423

Ho P. T. P. et al., 2009, ApJ, 694, 1610

Hobson M. P., Maisinger K., 2002, MNRAS, 334, 569

Hoshino A. et al., 2010, PASJ, 62, 371

Huang C. et al., 2010, ApJ, 716, 758

Irwin J. A., Bregman J. N., Evrard A. E., 1999, ApJ, 519, 518

Jones C., Forman W., 1984, ApJ, 276, 38

Jones M. E. et al., 2005, MNRAS, 357, 518

Komatsu E. et al., 2009, ApJS, 180, 330

Lacey C., Cole S., 1993, MNRAS, 262, 627

Lancaster K. et al., 2007, MNRAS, 378, 673

LaRoque S. J. et al., 2003, ApJ, 583, 559

LaRoque S. J., Bonamente M., Carlstrom J. E., Joy M. K., Nagai D., Reese E. D., Dawson K. S., 2006, ApJ, 652, 917

Leccardi A., Molendi S., 2008, A&A, 486, 359

Liao Y. et al., 2010, ApJ, 713, 584

McCarthy I. G., Bower R. G., Balogh M. L., 2007, MNRAS, 377, 1457

Markevitch M., Forman W. R., Sarazin C. L., Vikhlinin A., 1998, ApJ, 503, 77

Marshall P. J., Hobson M. P., Slosar A., 2003, MNRAS, 346, 489

Mohr J. J., Mathiesen B., Evrard A. E., 1999, ApJ, 517, 627

Mroczkowski T. et al., 2009, ApJ, 694, 1034

Muchovej S. et al., 2007, ApJ, 663, 708

Peebles J., 1993, Principles of Physical Cosmology. Princeton Univ. Press, Princeton

Plagge T. et al., 2010, ApJ, 716, 1118

Pratt G. W., Böhringer H., Finoguenov A., 2005, A&A, 433, 777

Romano A. et al., 2010, A&A, 514, A88

Sadler E. M. et al., 2006, MNRAS, 371, 898

Saunders R. et al., 2003, MNRAS, 341, 937

Schmidt R. W., Allen S. W., 2007, MNRAS, 379, 209

Sehgal N. et al., 2011, ApJ, 732, 44

Staniszewski Z. et al., 2009, ApJ, 701, 32

Struble M. F., Rood H. J., 1999, ApJS, 125, 35

Sunyaev R. A., Zeldovich Y. B., 1970, Comments Astrophys. Space Phys., 2, 66

Sunyaev R. A., Zeldovich Y. B., 1972, Comments Astrophys. Space Phys., 4, 173

Swetz D. S. et al., 2011, ApJS, 194, 41

Tsuboi M., Miyazaki A., Kasuga T., Matsuo H., Kuno N., 1998, PASJ, 50, 169

van Weeren R. J., Röttgering H. J. A., Brüggen M., Cohen A., 2009, A&A, 505, 991

Vikhlinin A., Forman W., Jones C., 1999, ApJ, 525, 47

Vikhlinin A., Markevitch M., Murray S. S., Jones C., Forman W., Van Speybroeck L., 2005, ApJ, 628, 655

Waldram E. M., Pooley G. G., Grainge K. J. B., Jones M. E., Saunders R. D. E., Scott P. F., Taylor A. C., 2003, MNRAS, 342, 915

Waldram E. M., Bolton R. C., Pooley G. G., Riley J. M., 2007, MNRAS, 379, 1442

Wu J. et al., 2009, ApJ, 694, 1619

Zemcov M., Borys C., Halpern M., Mauskopf P., Scott D., 2007, MNRAS, 376, 1073

Zhang Y., Finoguenov A., Böhringer H., Kneib J., Smith G. P., Kneissl R., Okabe N., Dahle H., 2008, A&A, 482, 451

Zhang Y. et al., 2010, ApJ, 711, 1033

This paper has been typeset from a TEX/LATEX file prepared by the author.